Acta Materialia 231 (2022) 117856

Contents lists available at ScienceDirect

Acta Materialia

journal homepage: www.elsevier.com/locate/actamat

Full length article

In-situ irradiation-induced studies of grain growth kinetics of nanocrystalline UO_2

Zefeng Yu[a,*], Xinyuan Xu[a], Wei-Ying Chen[b], Yogesh Sharma[c], Xing Wang[a], Aiping Chen[c], Christopher J. Ulmer[a], Arthur T. Motta[a]

[a] Ken and Mary Alice Lindquist Department of Nuclear Engineering, The Pennsylvania State University, University Park, PA 16802, USA
[b] Nuclear Science and Engineering Division, Argonne National Laboratory, Argonne, IL 60439, USA
[c] Center for Integrated Nanotechnologies (CINT), Los Alamos National Laboratory, Los Alamos, NM 87545, USA

ARTICLE INFO

Article history:
Received 27 November 2021
Revised 24 February 2022
Accepted 16 March 2022
Available online 23 March 2022

ABSTRACT

The thermal conductivity of UO_2 fuel needs to be high enough to dissipate the heat generated from the fission reaction. Since grain size affects thermal conductivity and grain size can evolve with irradiation, it is critical to understand in-reactor UO_2 grain growth. Most studies of grain growth in UO_2 are based on thermally driven processes at elevated temperatures. However, studies have shown that grain growth can occur even at cryogenic temperatures by ballistic processes. Such irradiation-induced grain growth in UO_2 is yet to be studied. Advanced *in-situ* Kr ion irradiation and transmission electron microscopy were systematically performed on nanocrystalline UO_2 thin films at temperatures ranging from 50 K to 1073 K; grain growth was observed at all temperatures. A combination of manual and machine learning techniques was used to measure and plot grain size evolution against irradiation fluence at various irradiation temperatures. The machine learning method has significantly improved the analysis efficiency and reduced human labors. The grain diameter data were fitted using classical grain growth and thermal spike models to describe grain growth kinetics with and without irradiation effect. Grain growth during low temperature irradiation ($\lesssim$ 475 K) can be well described by the thermal spike model. Above 475 K, there were additional thermally assisted processes that further accelerate the grain growth. At the highest irradiation temperature about 1075 K, both irradiation-induced dislocation loops and cavities/bubbles were observed to form in the UO_2. The effects of irradiation-induced defects on grain growth kinetics are discussed.

1. Introduction

The performance of uranium dioxide (UO_2) nuclear fuel is affected by grain growth in service [1–3]. Grain size affects many of the critical mechanisms that can cause fuel performance degradation, including thermal conductivity decrease, fission gas release, swelling and fracture toughness. Both experimental and molecular dynamics (MD) simulation studies have shown that thermal conductivity of polycrystalline UO_2 decreases with smaller grain size due to enhanced grain boundary phonon scattering [4,5]. Since fission gases are released through grain boundaries, smaller UO_2 grains can lead to faster intergranular fission bubble growth and reduce the residual gas within the grains [6,7]. On the other hand, enlarged grain size tends to degrade mechanical properties, such as hardness and fracture toughness [8]. Such dependence on grain size is especially important for high-burnup structure (HBS), which has shown nano-crystallization at high Xe dose level due to accumulation of radiation-induced defects [9]. Therefore, the grain size effect on material properties has been a critical concern for nuclear fuel design.

The growth of polycrystalline material under isothermal annealing is a thermally activated phenomenon, especially at the high temperatures during reactor operation. Under a curvature-driven mechanism, the difference in curvature between the two grains establishes a pressure, which causes unbalanced fluxes of atoms to jump cross the grain boundary. Thus, the grain boundary migrates toward the center of the boundary curvature in order to minimize the total boundary area, and thus reduce the total free energy [10]. Classical grain growth kinetics often can be described by

$$D^n - D_0^n = Mt \quad (1)$$

where D is the measured grain diameter, D_0 is the initial grain diameter, n is growth rate, M is a parameter describing the grain boundary mobility, and t is the annealing time. The exponent n

* Corresponding author.
E-mail address: zefeng@psu.edu (Z. Yu).

https://doi.org/10.1016/j.actamat.2022.117856
1359-6454/

describes the growth rate, and is commonly found to be 2 for pure metals upon isothermal annealing [11]. For polycrystalline ceramics, such as UO_2, the value of n has been reported to be between 2 and 4, depending on the pore migration mechanism [12]. By fitting the grain diameter data into the classic grain growth model, an activation energy (E_a) for grain growth can be calculated for UO_2, ranging from less 1 eV to larger than 6 eV [12–23]. It is uncertain whether UO_2 really shows such a large span of activation energies depending on the solute doping content and porosity sizes or whether this range is simply a result of unreliable fitting parameters used in the various studies [32]. Knowing the activation energy for diffsion of UO_2 is critical for many simulations and models on reactor performance, and thus, needs to be clarified more.

Grain growth under irradiation is complicated because the interaction of energetic particles with the target atoms can create a supersaturation of point defects, which can lead to radiation-enhanced diffusion (RED) and radiation-induced segregation (RIS) to sinks [24,25]. Previous studies in [26,27] have further shown that in pure materials an athermal grain growth mechanism exists under irradiation that causes grain growth even at cryogenic temperatures.

In an effort to better understand whether such a grain growth occurs in UO_2, systematic *in-situ* ion irradiation and transmission electron microscopy (TEM) studies were performed on nanocrystalline UO_2 thin films at various temperature from cryogenic to elevated temperatures. A combination of manual and machine learning techniques was used to measure the grain diameter as a function of fluence and irradiation temperatures. Ex-situ characterizations were also performed on the irradiated samples to investigate if there were surviving irradiation-induced defects, such as defect clusters and dislocation loops, and whether impurity segregation to sinks occurs. Both the classical thermal grain growth model and the thermal spike model were applied to the experimental data in order to calculate the activation energy of grain growth in UO_2. Activation energies were calculated with irradiation and for thermal annealing in the absence of irradiation and are discussed to explain the fast irradiation-induced grain growth kinetics. Combining the videos of *in-situ* irradiation and results from fitting to grain growth models, the grain growth process and mechanism are determined.

2. Experiment

2.1. Material synthesis and crystal structure

Pulsed laser deposition (PLD) was used to grow UO_2 thin films on an electron transparent silicon nitride membrane (purchased from Norcada) at Center for Integrated Nanotechnologies, Los Alamos National Laboratory. The depleted UO_2 target was fabricated by a conventional ceramic cold pressing and sintering process. The base pressure of the PLD chamber was 1.2×10^{-7} Torr. Pulses from a KrF excimer laser (Lambda Physik LPX 300, λ= 248 nm, 1−5 Hz) were focused on a stoichiometric, depleted UO_2 target at a repetition rate of 4 Hz and at an energy density of 1.5 J /cm^2. The target-substrate distance was set at 5 cm. To obtain nano-sized grains, the films were grown at room temperature with an argon gas partial pressure of 100 mTorr. The detailed target and thin film synthesis conditions were described elsewhere [28].

Post-deposition TEM characterizations confirm that the film exhibits an equiaxed grain structure as shown in Fig. 1A–E) and the average grain diameter was measured to be 10 to 15 nm. The diffraction patterns from the as deposited samples could be indexed according to the fluorite crystal structure of UO_2 with a lattice parameter of a_0 = 5.471 Å [29]. The diffraction patterns taken in this study suggest that the grains in the as-deposited samples do not have an obvious preferential grain orientation (see Fig. 1C)). The high resolution (HR) TEM images shown in Fig. 1D-E) also confirm that the material has a UO_2 crystal structure and compacted nanograins.

2.2. In-situ *isothermal irradiation and annealing experiments*

In-situ grain growth experiments were performed at the Intermediate Voltage Electron Microscopy (IVEM)-Tandem facility at Argonne National Laboratory, where a linear ion accelerator with a 911 Danfysik ion source is coupled with a Hitachi 9000 TEM at 30° for simultaneous ion irradiation and electron imaging. The isothermal irradiation experiments were conducted using 1 MeV Kr^{2+} ions at a flux of 6.25×10^{15} ions/m^2/s to a maximum fluence of 7.1×10^{19} ions/m^2. The TEM sample holder has the capability of heating or cooling to control the irradiation temperature, which is continuously monitored by thermocouples attached to the specimen cup. The irradiation temperatures were held at constant temperatures ranging from 50 K to 1075 K. The irradiation was systematically paused at specific ion fluences to acquire TEM images under both bright field (BF) and dark field (DF) imaging conditions, at 50kX and 100kX magnifications, respectively. The experiments were also continuously filmed. The DF images were taken using either the {111} or {220} diffraction rings. *In-situ* annealing experiments were conducted using the same sample holder inside the same TEM, but without ion irradiation.

The Stopping and Ranging of Ions in Matter (SRIM) computer code has been used to simulate the ion irradiation in order to calculate irradiation damage in the units of displacements per atom (dpa). The number of thermal spikes created per ion (χ), and the average thermal spike energy (Q) values related to the irradiation cascade were calculated using the outputs (collison.txt) from SRIM, as needed to calculate the activation energy under the thermal spike model [27]. The displacement energies used were 40 eV for U and 20 eV for O [30], and the thickness of the UO_2 foil was set at 50 nm. The simulation was performed in the full cascade mode for 175,000 ions at 50 nm thickness [27]. The irradiation damage, and recoil energy spectra for U and O are shown in Fig. 2A) and B), respectively. The irradiation damage was calculated using phonon.txt from SRIM outputs and the NRT displacement model [31]. Total fluence of 7.1×10^{19} ions/m^2 was used. The fluence to dpa ratio is 6.04×10^{18} (ions/m^2)/dpa. The ion energy was selected so that most ions completed traversed the samples and only very few Kr ions (0.46% for a 50 nm thick film) ions were implanted. The dpa calculated by SRIM increases with depth until decreasing at the end due to sputtering of displaced atoms from the back surface. Near the back surface some of the displacement cascades will come out the back end so that less damage is tallied.

2.3. Post-irradiation characterization

The samples were further characterized ex-situ at the Materials Characterization Lab at Pennsylvania State University after the IVEM irradiation experiments. The FEI Helios 660 DualBeam system with integrated focused ion beam (FIB) and scanning electron microscope (SEM) was used to prepare the cross-sectional TEM lamella on a Cu grid. A Pt layer was deposited on the UO_2 thin film surface to preserve the area before lifting. A current of 2 nA:30kV was used during the FIB liftout process. Then, the TEM lamella was thinned down using 1 nA:30kV and all the way down to 10 pA:30kV until transparency under 10 kV secondary electron beam. A final 20 pA:5kV clean-up process was used to minimize the Ga damage during the thinning process. The major purposes of preparing the cross-sectional TEM lamella are to confirm the thin film thickness and to study whether there was chemical redistribution during *in-situ* irradiation.

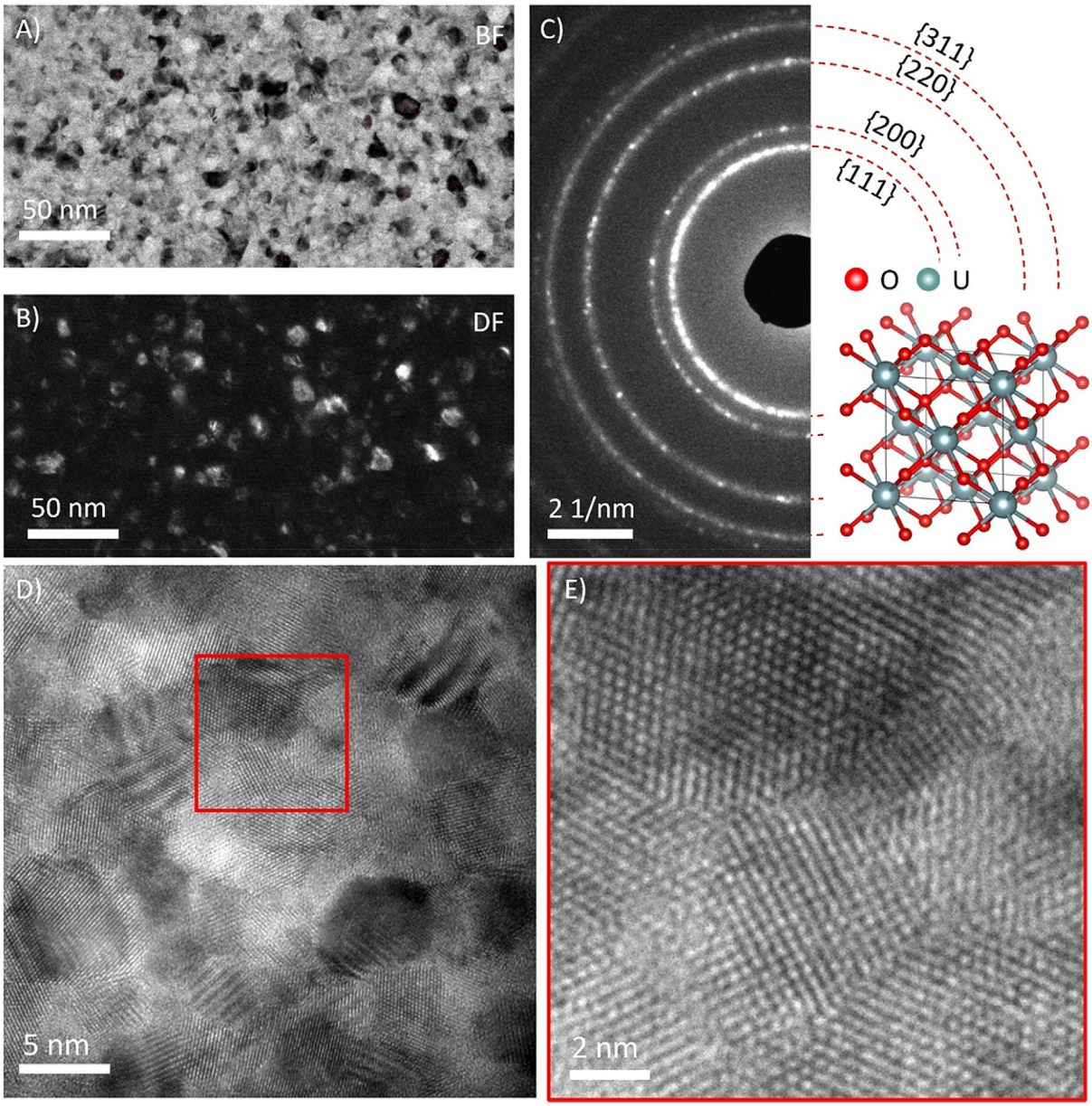

Fig. 1. The as-deposited UO_2 nanostructured films taken by TEM (A) bright-field (BF), (B) dark-field (DF), and (C) diffraction. The DF image was taken using the {111} diffraction ring. (D) and (E) HR-TEM image confirms that the material contains compacted nanograins.

Both 200kV FEI Tecnai G2 with LaB_6 electron gun and 200 kV FEI Talos F200X with X-FEG electron source and equipped with 'Super-X' Energy-Dispersive X-ray Spectroscopy (EDS) were used to study irradiation-induced defects and sample chemistry. A Bruker ESPRIT 2 detector was used for EDS acquisition and analysis. All EDS mappings shown in this study are relative intensity maps, i.e. no accurate quantification of the film composition was performed.

2.4. Grain diameter measurement

2.4.1. Manual method

To better obtain consistent and accurate grain diameter measurements from the TEM images, two methods were applied based on manual and machining learning techniques to identify and measure individual grains as a function of irradiation dose. The manual (M) method, illustrated in Fig. 3, is based on human observation to distinguish the grain shape and boundaries. Two lines across the identified grains were drawn and measured using ImageJ and the average of the two measured lengths were plotted as a function of fluence. To achieve good statics, the M method was applied to both 50–100kX BF and DF images at different fluences for each sample. Over 400 images were processed in this time-consuming manner.

2.4.2. The machine learning (ML) technique based on DF TEM images

To obtain statistically reliable results regarding grain growth, it is necessary to analyze a large number of grains under each irradiation condition. Therefore, a machine learning model that can automatically recognize and measure grains in TEM images is highly desired to save the time and to reduce the variation of imaging analysis. We have developed such a model using a specific convolutional neural network (CNN) called U-Net. U-Net has a unique U-shaped architecture with a contracting path to extract image context and a symmetric expansive path to propagate context information to higher resolution layers, which makes it efficient in image segmentation with very few training images [32]. In our model, five encoder blocks are used in the contract-

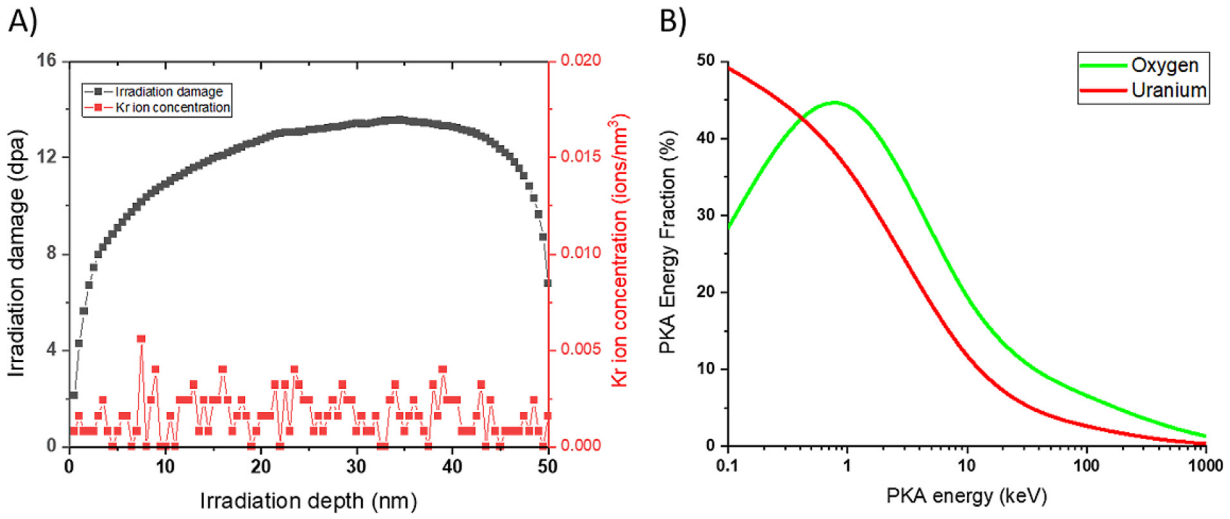

Fig. 2. (A) Irradiation damage and Kr ion concentration after a fluence of 7 × 10^{19} ion/m^2, and (B) recoil energy spectrum calculated using SRIM.

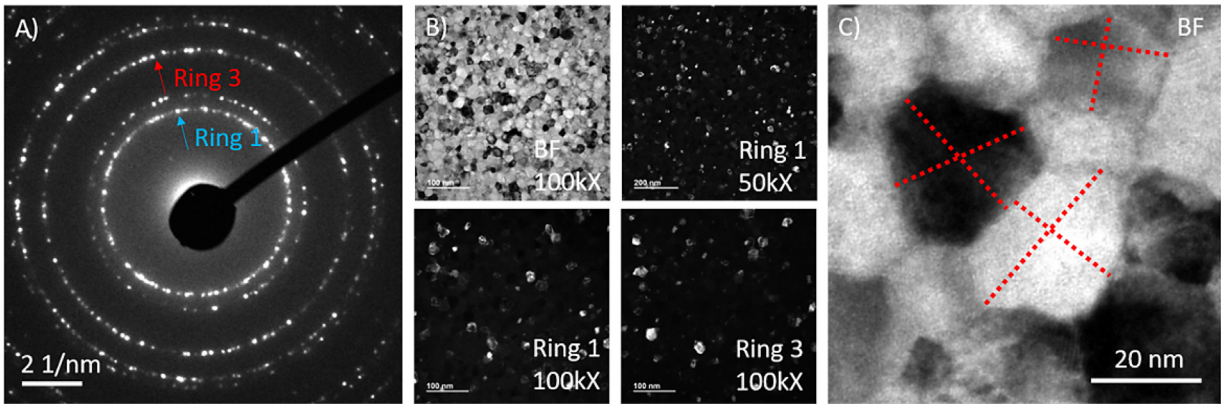

Fig. 3. Irradiated UO_2 thin film at 7.1 × 10^{19} ions/m^2 taken as (A) diffraction pattern and under (B) BF and DF conditions. Ring 1 corresponds to the {111} plane and ring 3 to the {220} plane of the UO_2 structure. (C) Manual measurement of the grain diameters on BF image. The red dotted lines represent some of the measured grain diameters.

ing path to extract the deep information contained in the original TEM images and then five decoder blocks are used to concatenate up-sampling images with the left feature images. Finally, a 1 × 1 convolutional output layer is used to map two feature vectors to the desired classes, i.e., “grain” and “non-grain”. In total, one input layer, one output layer, four max-pooling layers, four concatenate layers and 23 convolutional layers are used in the network.

Because a limited number of manually labeled DF TEM images were available for training the U-Net model, data augmentation was essential to enlarge the training dataset for a more robust model. In this project, we used 20 DF TEM images of 1024 × 1024 pixels as the original training dataset. Common augmentation methods, including rotation, zooming, and shearing were applied, so the final training dataset contained 200 images. The augmentation improved the precision from 81.62% to 86.85%, the recall from 72.81% to 76.15% and the F1 score from 76.96% to 81.15%. The precision (P) means the percentage of real grains identified by U-Net of all real grains in ground truth. Recall (R) means the percentage of real grains identified by U-Net of all the "grains" identified by U-Net. F1 score is equal to 2PR/(P + R), so it indicates the overall performance of the machine learning model. We used a NVIDIA Tesla P100 GPU to train the model to 200 epochs with L2 Regularization. The training was terminated when the validation loss became stable. The total training time was about six hours.

3. Result and discussion

3.1. Comparison of measured grain diameters by two methods

To demonstrate the effectiveness of the ML method, we compared an original TEM image of the sample irradiated at 50 K up to 7 × 10^{19} ions/m^2 in Fig. 4(A) to the same image processed by ML method in Fig. 4 (B). As the figures show, the grains identified by the ML method match quite well with the grains shown in the original images. To ensure consistent and accurate measurements of grain diameters at different imaging conditions and at each irradiation fluence, the averaged grain diameters measured by the M and ML methods are plotted in Fig. 4(C) for low temperature (T = 50 K) irradiation experiments and D) for high temperature (T = 675 K) irradiation experiments, as two examples. The error bars represent the standard deviation (stvd) of all the grain diameters measured from TEM images. Despite the analysis being performed using images obtained using different magnification and diffraction conditions, all the methods show relatively large stvd, (about 40 % of the measured grain diameters) at each irradiation fluence. On the other hand, since all methods result in similar stvd values, it demonstrates the great consistency between using different methods. This is expected, since large grains tend to grow at the expense of the smaller grains which exhibit with large grain boundary curvature. This can result in large stvd.

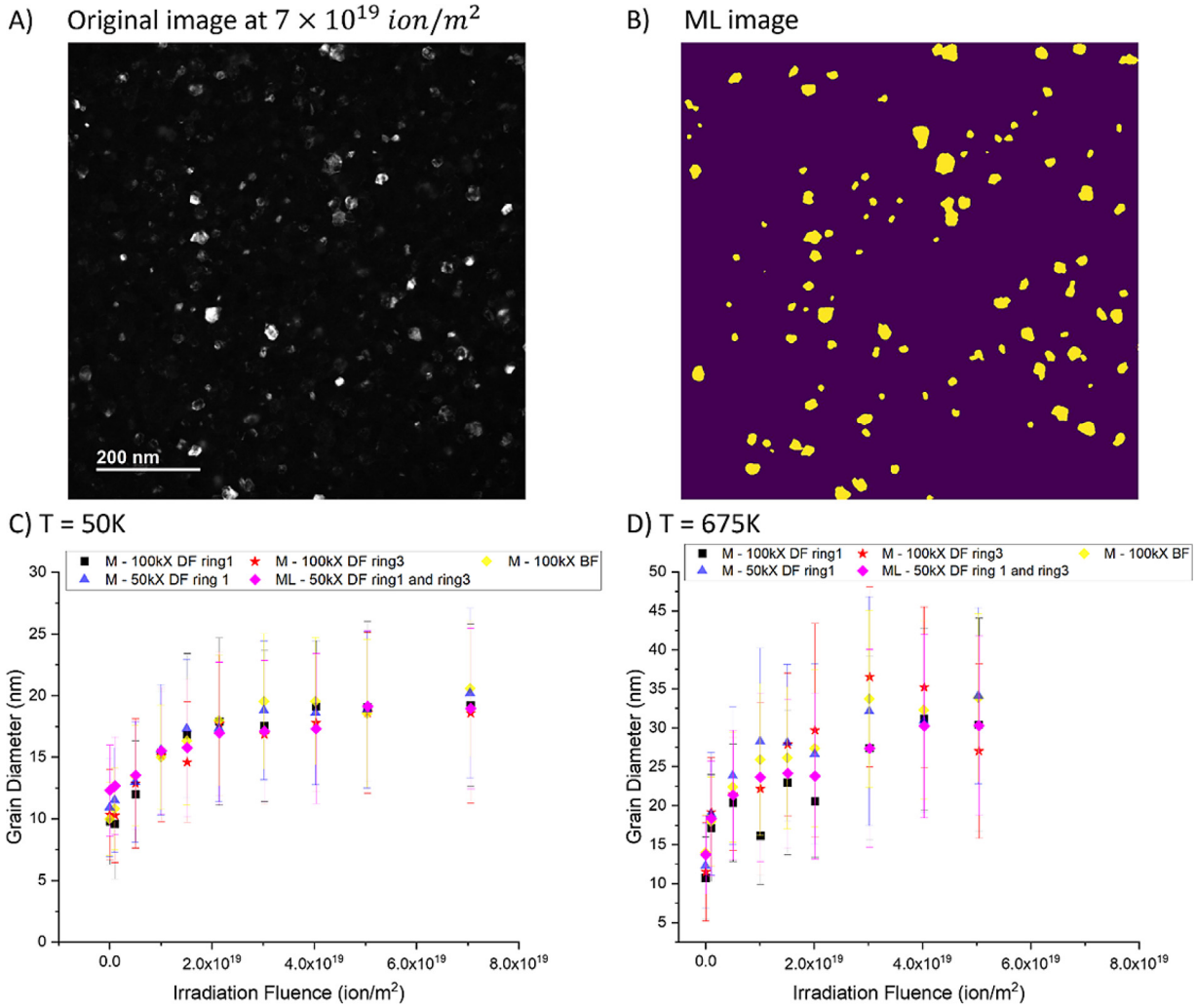

Fig. 4. Original DF image taken for a sample irradiated at 50 K up to 7×10^{19} ion/m^2. (B) Image processed by the ML method to identify the grains in yellow color. (C) Grain diameters measured using both BF and DF TEM images as a function of irradiation fluences at irradiation temperatures of 50 K and (D) 675 K. "M" represents the manual method, whereas "ML" represents the machine learning method. The results using ML method correspond to the average grain diameters based on DF images acquired with objective aperture located at diffraction ring 1 and ring 3. (For interpretation of the references to color in this figure, the reader is referred to the web version of this article).

On the other hand, the average grain diameters measured by each method are quite consistent with each other. For example, there are five average grain diameters at each irradiation fluence plotted for the 50 K irradiation experiments in Fig. 4(A). The standard deviation of all the average grain diameters at the same fluence is less than 1 nm (3-10% of the grain diameter). As the grains grow and less grains are counted, this standard deviation increases but are still relatively small. The agreement between the two methods shows that, once properly trained and with strictly defined grain identification criteria on low magnification images, the ML method can provide high-throughput analysis and reliable statics. Thus, all the grain diameters shown in the rest of this study were measured by the ML method and used to fit the grain growth equations.

3.2. Isothermal grain growth without irradiation

In order to understand the effect of irradiation on grain growth, it is necessary first to separate the thermal contribution to the grain growth. This was done by quantifying the grain growth at various temperatures without irradiation. In this study, isothermal annealing experiments were performed at temperatures ranging from 475 K to 1075 K, as shown in Fig. 5. At 475 K, no thermally driven grain growth was observed after a 5 hr anneal. Some grain growth was seen after a 1.5 hr anneal at 675 K. At the highest annealing temperature (1075 K), the nanocrystalline grains grew to the largest size, about 25 nm, at the end of the anneal, as shown in Fig. 5(A). To compare the thermally driven grain growth rates at various temperatures, the grain diameters after annealing at different temperatures are plotted in Fig. 5(B). The grain diameters measured by both the M and ML methods are plotted in the same figure and show good agreement. Although the grain growth rate increases with temperature, the grain diameters start to saturate after about 1 hr annealing and little grain growth can be observed afterwards.

The dashed lines in Fig. 5(B) are fitted curves based on the ML results. Eq. (1) was used for the fitting. Both n and M are variables fitted to experimental data at each temperature. Although n has been reported to be 2 to 4 based on the porosity migration mechanism involved during the thermal grain growth [12,19] in this study, the best fit value of n at all temperatures to describe the grain growth kinetics is greater than 14. This high value of n does not have a physical meaning. If on the other hand, n is fixed to either 2 or 3, it is not possible to capture the saturating grain growth behavior seen in Fig. 5(B) using Eq. (1). Other grain growth models, such as described in [11,33], have considered an extra retarding

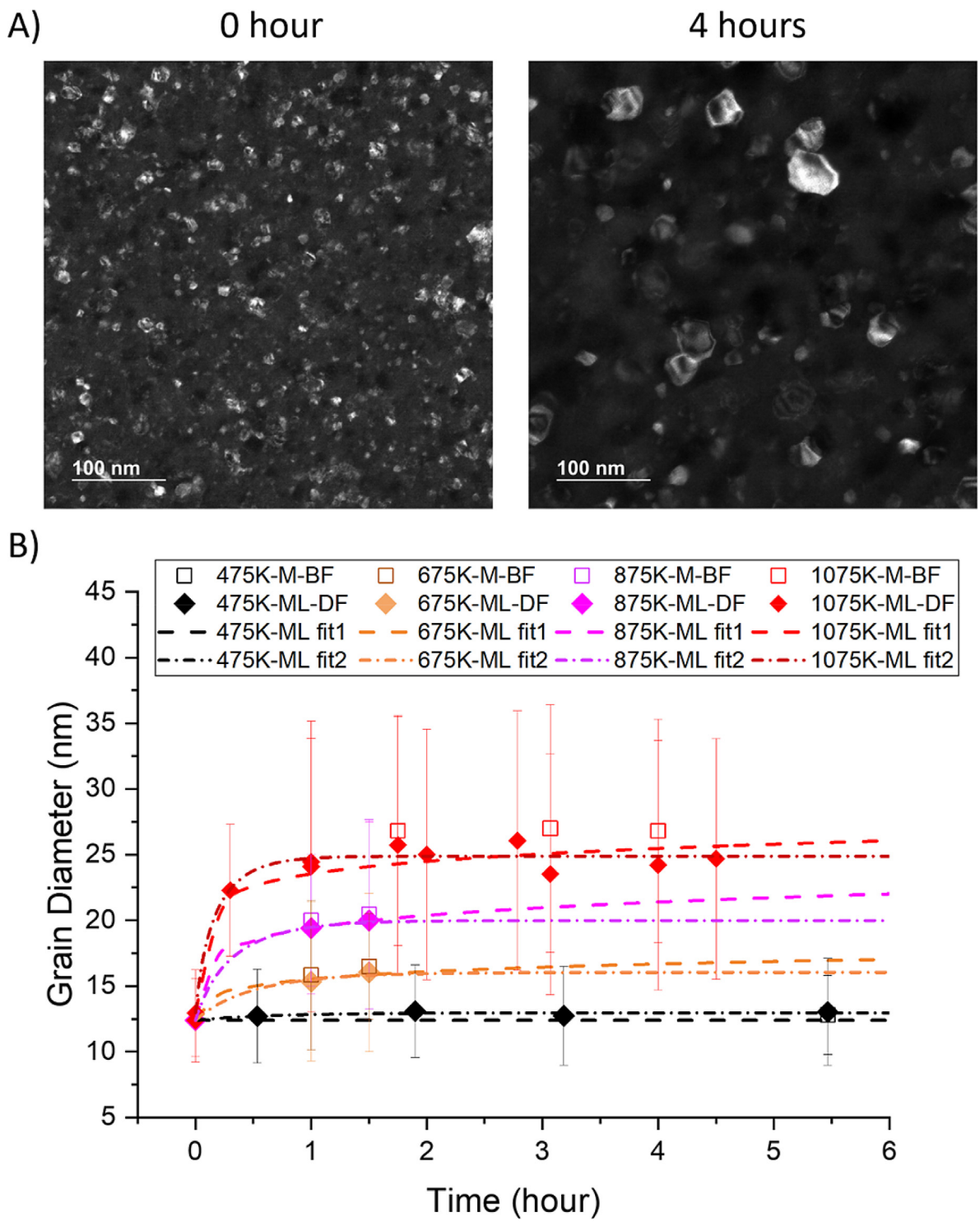

Fig. 5. (A) DF TEM images showing initial grain diameters and after annealing without irradiation at 1075 K for 4 hr. (B) Summary of isothermal grain diameter during annealing at various temperatures. The dashed lines are best fits using Eq. (1) and Eq. (2), respectively. "fit1" means numerically fitted data using Eq. (1). "fit2" means numerically fitted data using Eq. (2).

force (ex. solute drag effect and the presence of porosity) pinning the grain boundaries and leading to a plateau regime. Thus, these modified equations may better describe the grain growth kinetics in this study. The equation including the extra force is

$$\frac{dD}{dt} = A\left(\frac{1}{D} - \frac{1}{D_{max}}\right) \quad (2)$$

where D_{max} is the measured maximum grain diameter and A is a fitted parameter. Numerical solutions were obtained by setting the fitting parameter A to Eq. (2) at four different temperatures and are plotted as "fit2" in Fig. 5(B). This fit captures the plateau region quite well. It is important to point out that in the absence of the extra force term ($A/D_{max} = 0$ or D_{max} = infinite in Eq. (2) becomes equivalent to Eq. (1) with n = 2. Although this has not been verified and it is not clear why that should be the case, the limit

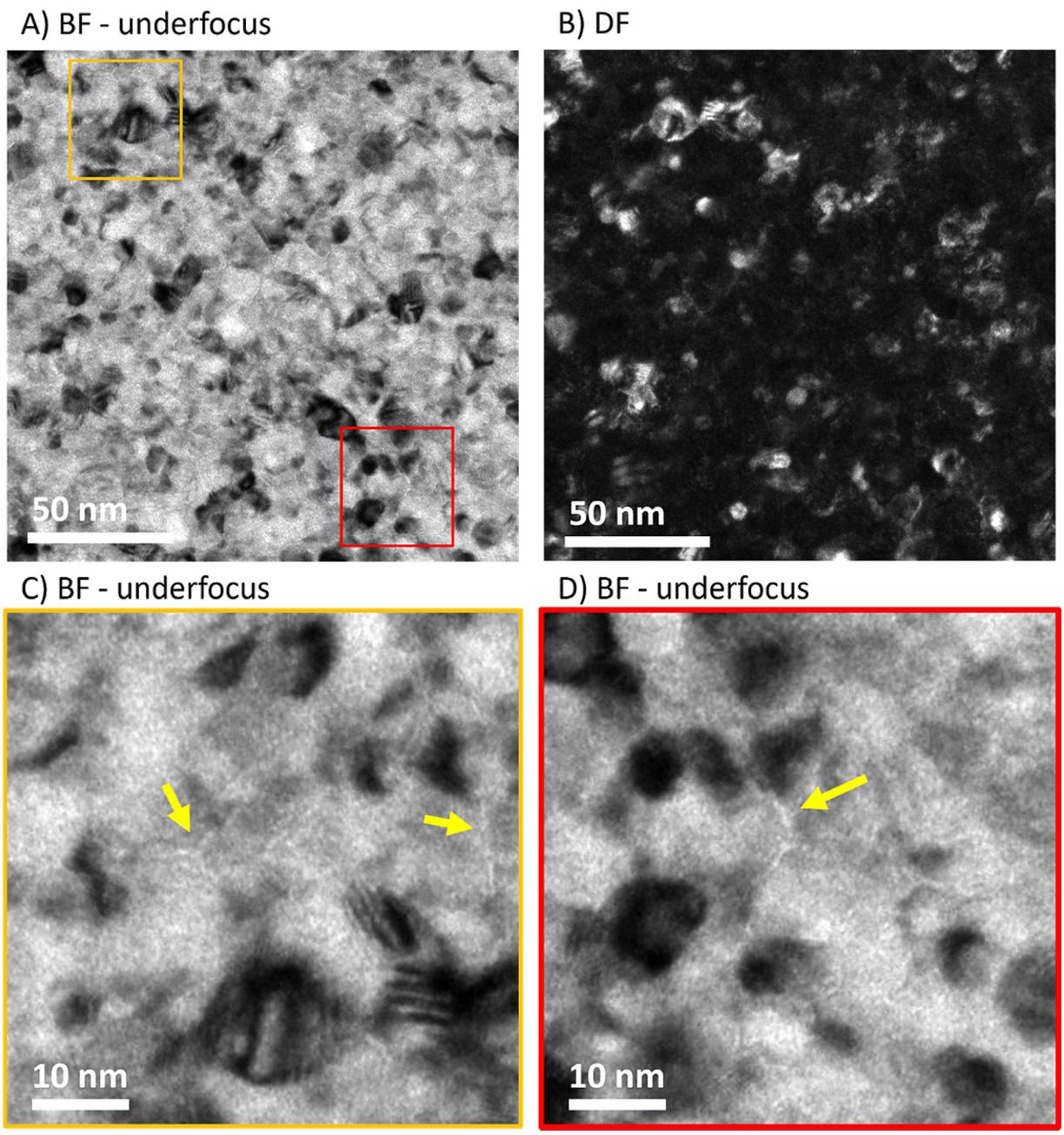

Fig. 6. (A) Underfocus BF image and (B) DF image of as-deposited UO_2 thin films. (C) and (D) Underfocus BF image at high magnification showing the nano-porosities (pointed by the yellow arrows) at grain boundaries. (For interpretation of the references to color in this figure, the reader is referred to the web version of this article).

of the diameter growth coincides approximately with the sample thickness, so that is used as D_{max} value. Therefore, the growth rate in this study still follows the classical thermal grain growth kinetics, but with an extra pinning force. Tonks et al. also pointed out that the A term, which is the rate constant, is equivalent to $a\bar{M}\bar{\gamma}$, where a is a geometric constant, $\bar{M}$ is the grain boundary mobility and $\bar{\gamma}$ is the grain boundary surface energy [2]. $\bar{M}$ and $\bar{\gamma}$ can be further described as

$$\bar{M} = M_0 \exp\left(-\frac{Q^{th}}{RT}\right) \quad (3)$$

$$\bar{\gamma} = \left(1.56 - 5.87 \times 10^{-4}T\right) \quad (4)$$

where Q^{th} is the thermally induced activation energy for grain boundary motion, R is the gas constant and T is the temperature. The pre-exponential term M_0 was calculated to be 2.14×10^{-7} $m^4/J/s$ and $a = 1$ (in [2]). Using the fit of the 1075K data in this study to determine A, Q^{th} was calculated to be 2.45 eV for our samples. This result is relatively close to the literature value, which is 3.01 ± 0.23 eV [2].

Since the sample composition in this study is well controlled during deposition under vacuum, it is unlikely that significant impurities are present. Also, no second phase particles were observed in the UO_2 thin films that could retard grain growth. On the other hand, the presence of porosity at grain boundaries is common in synthesized thin films. To investigate if there are porosities in our samples, one of the as-received samples was imaged in the underfocused BF condition. Fig. 6(A-B) shows compacted nanograins of as-deposited thin films at relatively low magnification. However, higher magnification images clearly show nano-pipe like porous structures at the grain boundaries as indicated. Thus, the TEM re-

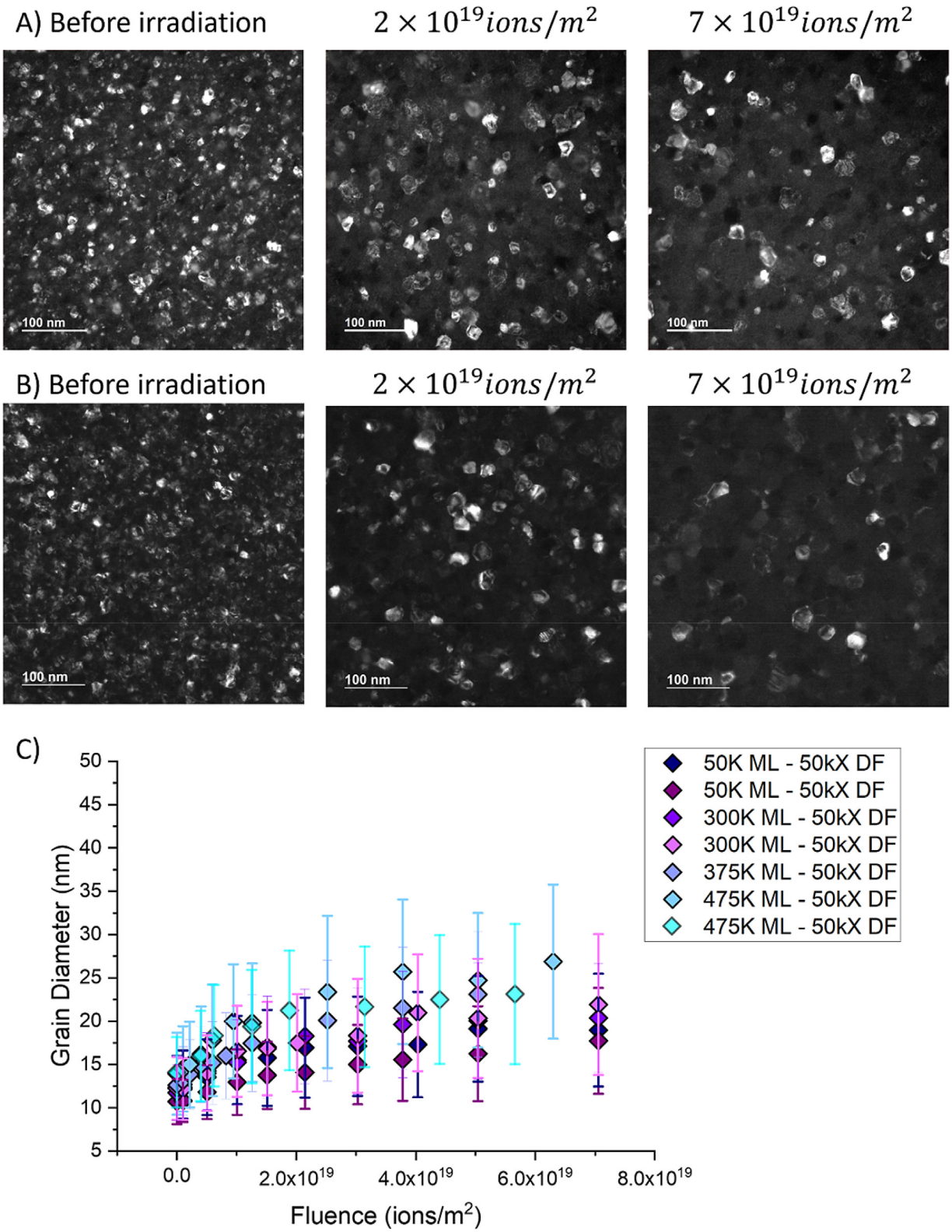

Fig. 7. DF TEM images of grain growth at (A) 50 K and (B) 475 K, respectively. (C) The grain diameter (as measured by the ML method) for irradiation temperatures ranging from 50 K to 475 K. The error bars correspond to the standard deviation of the measured grain diameters.

sults confirms that some amount of nanoporosity is present at the grain boundaries of the as deposited UO_2 thin films. Since irradiation can also induce porosities/bubbles/cavities in the materials, the effect on porosity on film behavior can be more significant under irradiation.

3.3. Irradiation induced grain growth

3.3.1. Low temperature grain growth

The grain growth kinetics observed at various irradiation temperatures are separated into two regimes. The grain growth rates

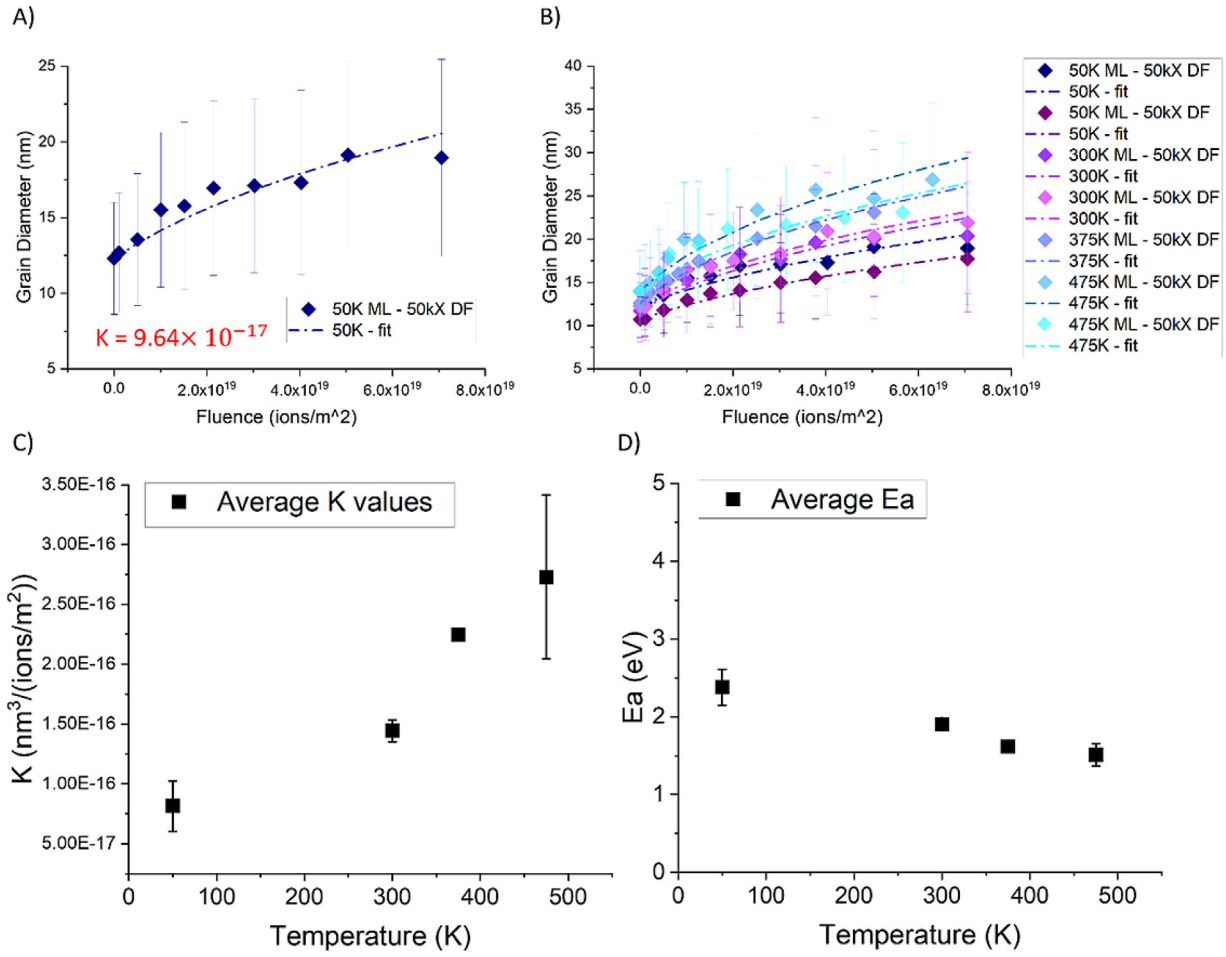

Fig. 8. Data fitting to obtain the growth rate, K, for (A) 50K irradiation and (B) all irradiation temperatures. (C) Fitted K values as a function of temperature. (D) Activation energy calculated from the fitted K values. The error bars are the standard deviation of the values calculated from two datasets at the same temperature.

observed during irradiation at temperatures up to 475 K are considered to be within the low temperature grain growth regime, whereas irradiation at temperatures higher than 475 K are considered to be within the high temperature grain growth regime. The irradiation temperature of 475 K was chosen as the boundary of the two regimes because isothermal annealing experiments without irradiation at 475 K for 5 hr show little thermally driven grain growth but annealing at higher temperatures does show obvious grain growth, as illustrated in Fig. 5(B).

As already shown in Fig. 4(A), grain growth clearly occurs at cryogenic conditions, where thermally driven grain growth does not occur. To illustrate low temperature grain growth, DF TEM images at three different fluences are shown in Fig. 7A), which clearly demonstrates grain growth at high irradiation fluences. Fig. 7(B) shows that grain growth observed in samples irradiated at 475 K is a little higher, but similar to that seen at 50 K. Fig. 7(C) summarizes the grain diameters (measured by the ML method) within the low temperature regimes from 50 K to 475 K. The measurement confirms that the nanocrystalline UO_2 grains have indeed grown within the low temperature regime under irradiation. Although the thermal effect from low temperature sample heating on the grain growth is expected to be minimal, grains still grow slightly faster during irradiation at 475 K than during irradiation at lower temperatures. The final average grain diameters observed during the 475K irradiation are the largest in the low temperature regime. One of possible reasons to explain the higher grain growth for the sample irradiated at 475 K compared to 50 K is related to the temperature effect on the size of the thermal spike created during the cascade. As pointed out by Kaoumi et al. in [34], the term d_{spike} is the diameter of the thermal spike, which can increase with increasing bulk material temperature . A larger d_{spike} leads to faster grain growth because of a larger probability of interaction between the thermal spike and the grain boundary. In the irradiation of thin films, the role of the free surface could be a concern as it would absorb point defects. However, the initial grain size is much smaller than the foil thickness so that point defects created during irradiation are much more likely to encounter grain boundaries than the free surface. In addition, similar work by Kaoumi et al. in [26,27] saw no effect of foil surface on grain growth because the low temperature irradiation is within the recombination dominated regime. The fact that the grains grow during irradiation is observed and can be rationalized with the current understanding.

3.3.2. *Data fitting and calculation of* E_a^{spike} *in the low temperature regime*

One of the goals in this study is to check whether the thermal spike model developed by Kaoumi et al. in [27] can be applied to describe the grain growth kinetics of UO_2 thin films. The governing equation of thermal-spike-driven grain growth is

$$D^3 - D_0^3 = K\phi t \quad (5)$$

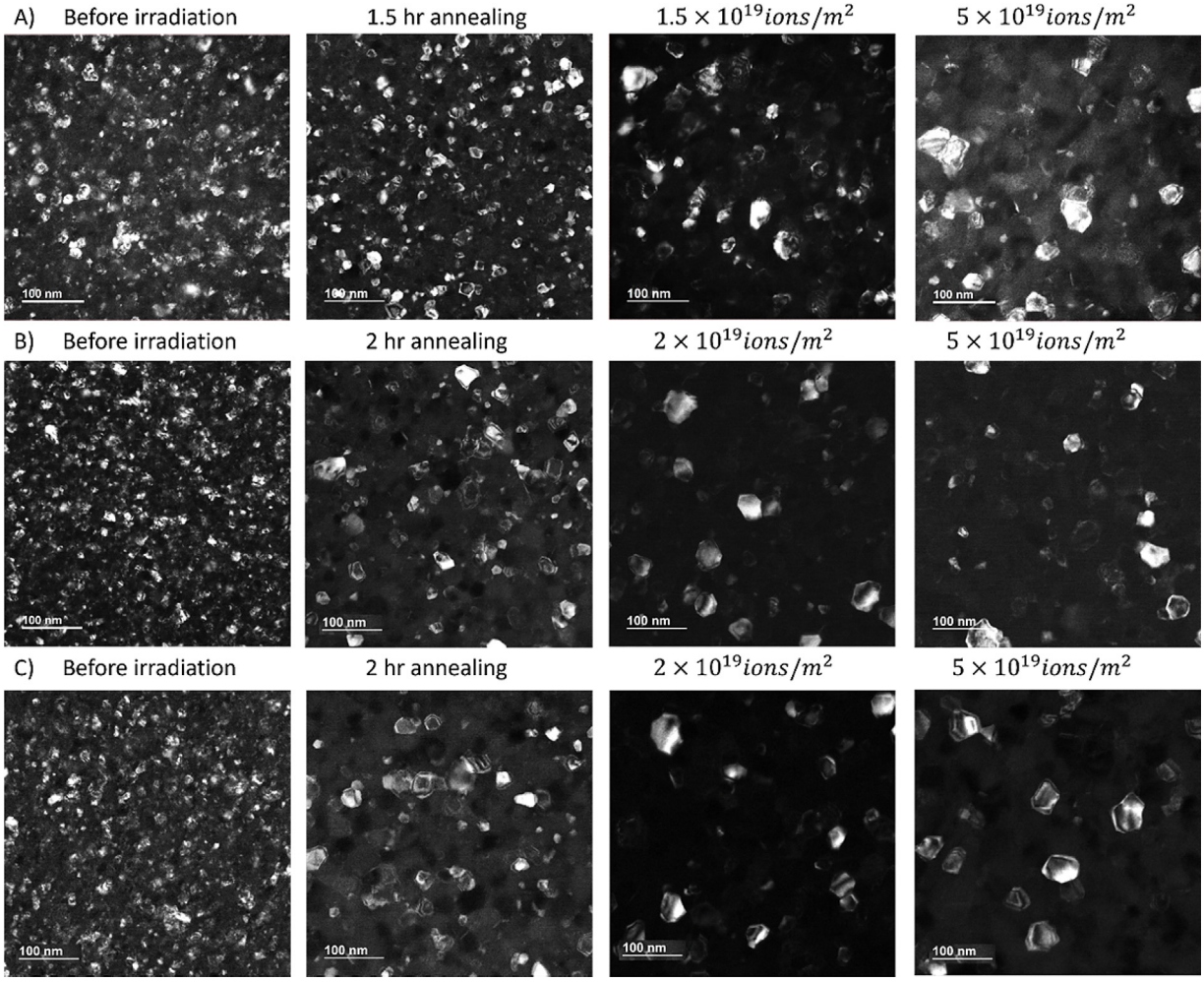

Fig. 9. DF TEM images of UO_2 thin film irradiated at (A) 675 K, (B) 875 K and (C) 1075 K. In each case, before irradiation, after a 2 h anneal, and then irradiated after the specified dose.

$$K = \frac{36\gamma d_{spike} X \delta V_{at} v \sqrt{\frac{3}{5}} \Gamma\left(\frac{8}{3}\right) k_B^{\frac{5}{3}}}{10\pi C_0^{2/3} k_0} \frac{Q^{5/3}}{\left(E_a^{spike}\right)^{8/3}} \quad (6)$$

where D_0 is the initial grain diameter, ϕ is the ion flux (ions/m^2/s), t is time (s), and K is the growth rate (nm^3/(ions/m^2)), obtained from fitting the measured grain diameters into Eq. (5) [27,35]. Then, the obtained K values are used to calculate the activation energy, E_a^{spike}, in the thermal spike regime.

Fig. 8(A) shows least squares fit to the data to obtain the grain growth rate, K, during Kr ion irradiation at 50K. The fitted curve closely follows the measured data (the least squares error is less than 10). The same fitting procedures were applied to the other low temperature irradiation experiments, as shown in Fig. 8(B), and the corresponding fitted K values are plotted in Fig. 8(C) as a function of temperature. The data indicates that the grain growth rate increases as a function of irradiation temperature.

The next step is to calculate the E_a^{spike} using Eq. (6). The parameters used are described in Table 1 and in the Appendix Figs. A1–A3. Since grain growth by the thermal spike model is attributed to the atomic jumps occurring within the thermal spike, it is reasonable to assign the relevant variables (such as γ, C_0 and k_0) as the value near the melting temperature of UO_2. In this circumstance, the fitted K is the only changing variable at different irradiation temperatures. Although the activation energy should be temperature independent, the resultant E_a^{spike} shows an apparent decrease with increasing growth rate. At 50 K, the E_a^{spike} is about 2.4 eV in average and decreases to about 1.5 eV at 475 K. One possible reason for this change is that d_{spike}, increases with increasing bulk temperature. The bulk temperature increases the thermal spike lifetime and size, and thus the number of jumps in it. This increase should be taken into account for the calculation of E_a^{spike}. However, in order to fit the results at 475 K using an activation energy of 2.4 eV, the d_{spike} would need to be increased from 9.3 nm at 50 K to 27 nm at 475 K, which is likely excessive. It is possible that some residual thermal effect at low temperature irradiation accelerates the growth rate, K, at 375 and 475 K, which should be further investigated. It is extremely important to point out that the Q^{th} calculated previously under thermal effect is consistent with the E_a^{spike} value at 50 K irradiation using the thermal spike model. Therefore, the E_a^{spike} calculated at 50K should be considered as the accurate activation energy to initiate atomic jumps between the grain boundaries under the sole influence of irradiation .

3.3.3. High temperature grain growth

The results of the grain growth experiment under isothermal annealing confirm that significant thermally driven grain growth occurs for annealing temperatures higher than 475 K. DF TEM images in Fig. 9(A)–(C) show the grain diameters before and after isothermal annealing at 675 K, 875 K, and 1075 K, respectively.

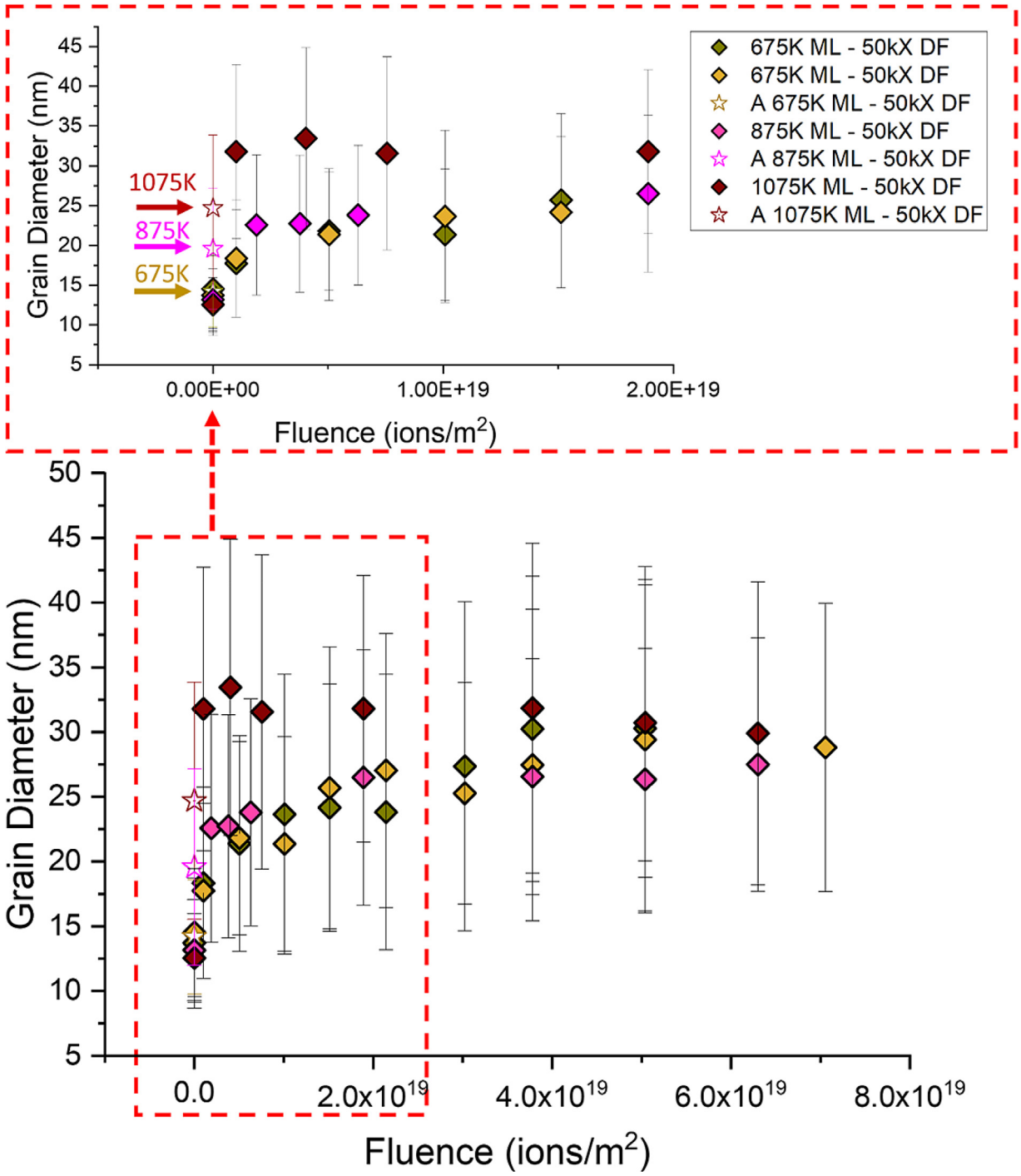

Fig. 10. Summary of grain growth under irradiation and simple annealing at the higher temperatures. Colored solid arrows point to the grain diameters after annealing at three different temperatures, respectively. "A" represents the grain diameters after long isothermal annealing.

The grain diameters at the end of the thermal annealing at the temperatures indicated are shown by the solid and colored arrows in Fig. 10, which are consistent with the long-time annealing data plotted in Fig. 5(B). Significant grain growth still occurred as a result of irradiation at the intermediate temperatures of 675 K and 875 K, after the samples had been annealed for more than an hour before irradiation. This suggests that although the grain diameter has almost achieved equilibrium under thermal annealing, ion irradiation can further increase the average grain diameter. Therefore, grain growth at elevated temperatures relative to the initial as-received thin films (without annealing and irradiation) is a combination of thermal and irradiation-driven processes. At the highest temperature of 1075 K, the extra grain growth induced by irradiation is less than that at 675 K and 875 K. The irradiated sample at 1075 K quickly reaches saturation grain diameter of about 30 nm as soon as irradiation starts. This is possibly due to the large grain diameter achieved after thermal annealing, which significantly decreases the probability of intersection of the thermal spikes with grain boundaries. Another possible reason is due to the resistive force, such as irradiation-induced porosities, which can pin the grain boundary motion. High temperature irradiation are within sink dominated regime [27]. Free surface and grain

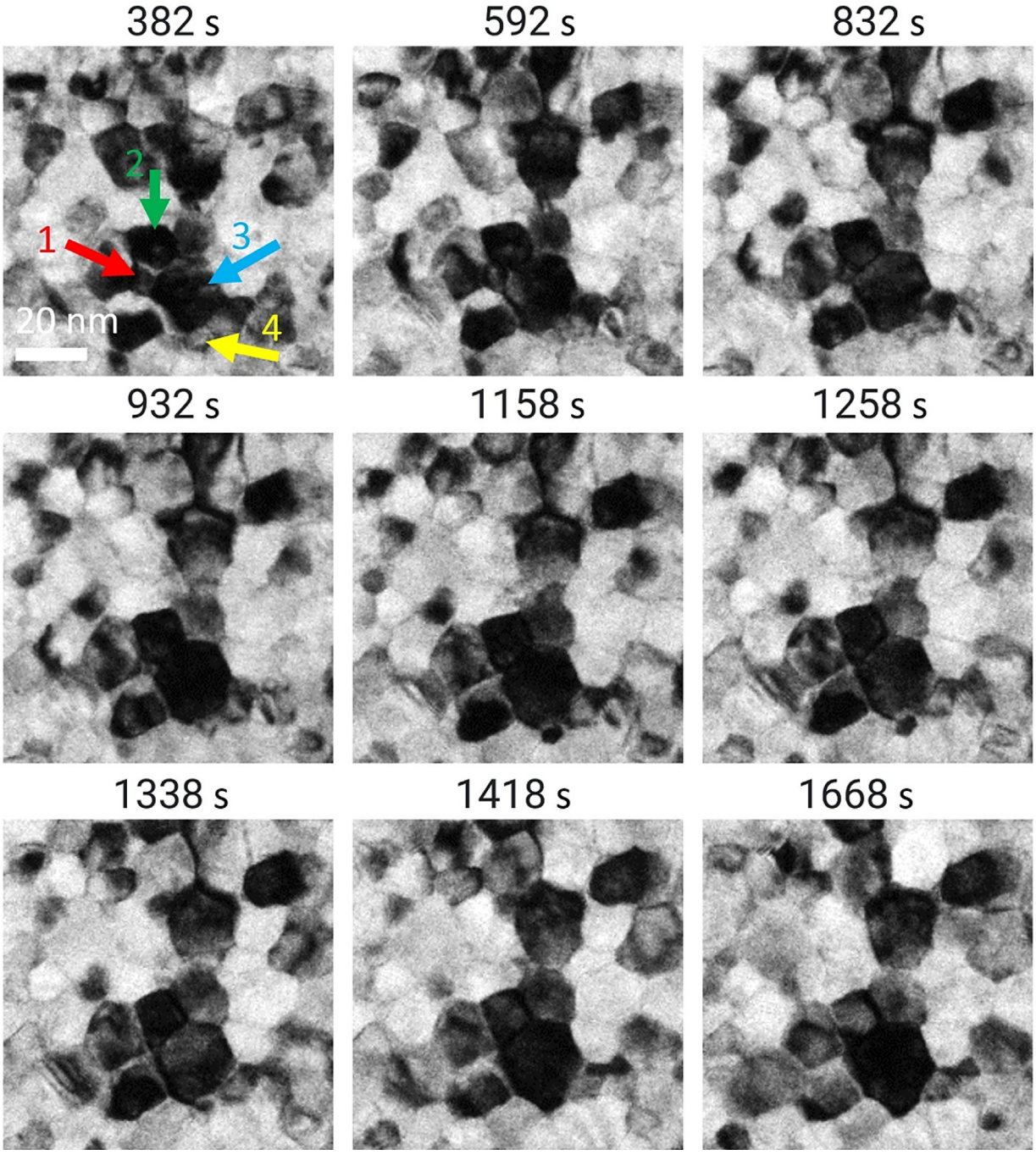

Fig. 11. BF TEM images taken from video during *in situ* experiment showing the grain growth processes at 300 K as a function of irradiation times. The time label here starts from the start of the irradiation. The solid arrows point to different grains. The dose rate is 6.25 $\times$ 10^{15} ions/m^2/s.

Table 1
The description and literature values of the variables needed to calculate the thermal spike grain growth kinetic parameter K for UO_2 thin film.

Parameters	Variables	Values	Refs.
grain boundary surface energy	γ	1 (J/m^2)	[1,2,36–41]
thermal spike diameter	d_{spike}	9.63 (nm)	[27,35]
thermal spikes per ion	X	0.0407 (spikes/ion/nm)	[27,35]
grain boundary width	δ	0.6 (nm)	[27,35]
atomic volume	V_{at}	0.0136 (nm^3/atm)	[27,35]
Debye frequency	ν	2.20 (THz)	[42]
Boltzmann constant	k_B	8.62 $\times 10^{-5}$ (eV/K)	[27,35]
average thermal spike energy	Q	25.27 keV	[27,35]
heat capacity	C_0	213.96 (J/mol/K)	[43–51]
thermal conductivity	k_0	3 (W/m K)	[42,48,51–59]

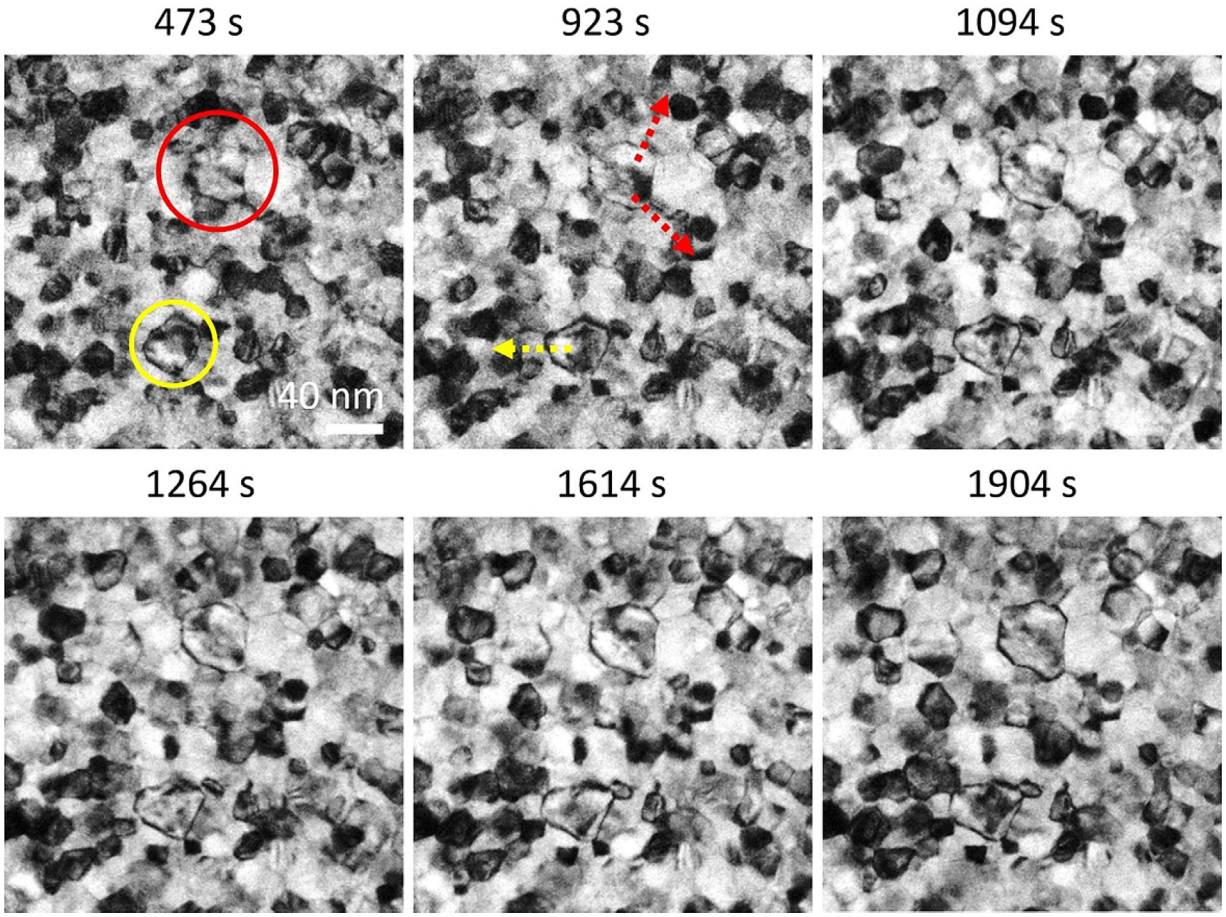

Fig. 12. TEM images taken from video showing the grain growth processes at 675 K as a function of irradiation time. The time label here indicates the time since the start of irradiation. The solid circles highlight the grains for analysis. The dashed arrows point to the grain growth direction.

boundaries are strong sinks for point defects, which can affect the evolution of irradiation-induced defects (dislocation and porosity/void). If interstitials generated by the irradiation can escape to the free surface and grain boundary, the leftover vacancies can trap Kr ions to form Kr bubbles [60] that can retard grain boundary mobility. The irradiation-induced defects formed in the 1075 K irradiated sample, can also affect grain growth, as discussed in below.

The thermal spike model was initially developed for low temperature irradiation conditions, in which no thermal grain growth occurs. Thus, it is not proper to directly apply the thermal spike model to experimental data under high temperature irradiation, and as a result the calculated $E_a^{spike}$is about 1 eV by keeping other parameter values the same as used for low temperature irradiation. E_a^{spike} is not expected to be a temperature dependent parameter. Therefore, the thermal spike model should be further modified to fully take into account the thermally assisted processes.

3.4. In-situ *observation of grain growth process*

Although grain diameters can be measured using static TEM images acquired at fixed irradiation fluences, it is not possible to directly observe the dynamic grain growth process. The *in-situ* TEM experiment allows us to take TEM images every second during the irradiation, enabling us to track the movement of individual grain boundaries to better understand the grain growth process in real-time. In this section, *in-situ* videos of both low and high temperature irradiated samples were analyzed. The series of BF TEM images show the selected frames demonstrating the grain growth process for the 300K irradiated sample in Fig. 11 and 675 K irradiated samples in Fig. 12. In Fig. 11, four neighboring grains are marked by four arrows in different colors. As the time progresses, the relatively smaller grain 1 pointed by the red arrow shrinks in size and seems to be “eaten” by the neighboring bigger grains 2 and 3. Similarly, the small grain 4 also shrinks in size as the irradiation progresses and eventually becomes fully incorporated into the upper bigger grain 3. As a result, after 1286 s the diameter of grain 3 grows from 19.68 nm to 24.28 nm. During that time the average grain growth rate for this particular grain is about 3.57×10^{-3} nm/s from fluence $= 2.4 \times 10^{18}$ ions/cm^2 to 1×10^{19} ions/cm^2 fluence. A similar phenomenon happens during high temperature irradiation at 675 K. As shown in Fig. 12, we tracked the growth of two grains highlighted by the red and yellow circles. Initially, many small neighboring grains are found around or overlapping the big grain indicated in the circles. Later in the irradiation, the smaller grains have disappeared, and a clear growth of large grains can be observed along the directions pointed by the dashed arrows. The averaged grain growth rate for these two grains is about $5.08 \pm 2.65 \times 10^{-3}$ nm/s from 2.9×10^{18} ions/cm^2 to 1.2×10^{19} ions/cm^2 fluence. The slightly higher grain growth rate at 675K than the 300K irradiation is expected because of the extra thermally assisted processes. It is interesting to compare the individual growth rates for these grains with the overall (average) grain growth rates for the sample – we should expect those to be higher than the average. In this case, the individual grain growth rate during the time shown in Fig. 11 is 1.76 times higher than the average at 300 K and 2.04 times higher than the average at 675 K.

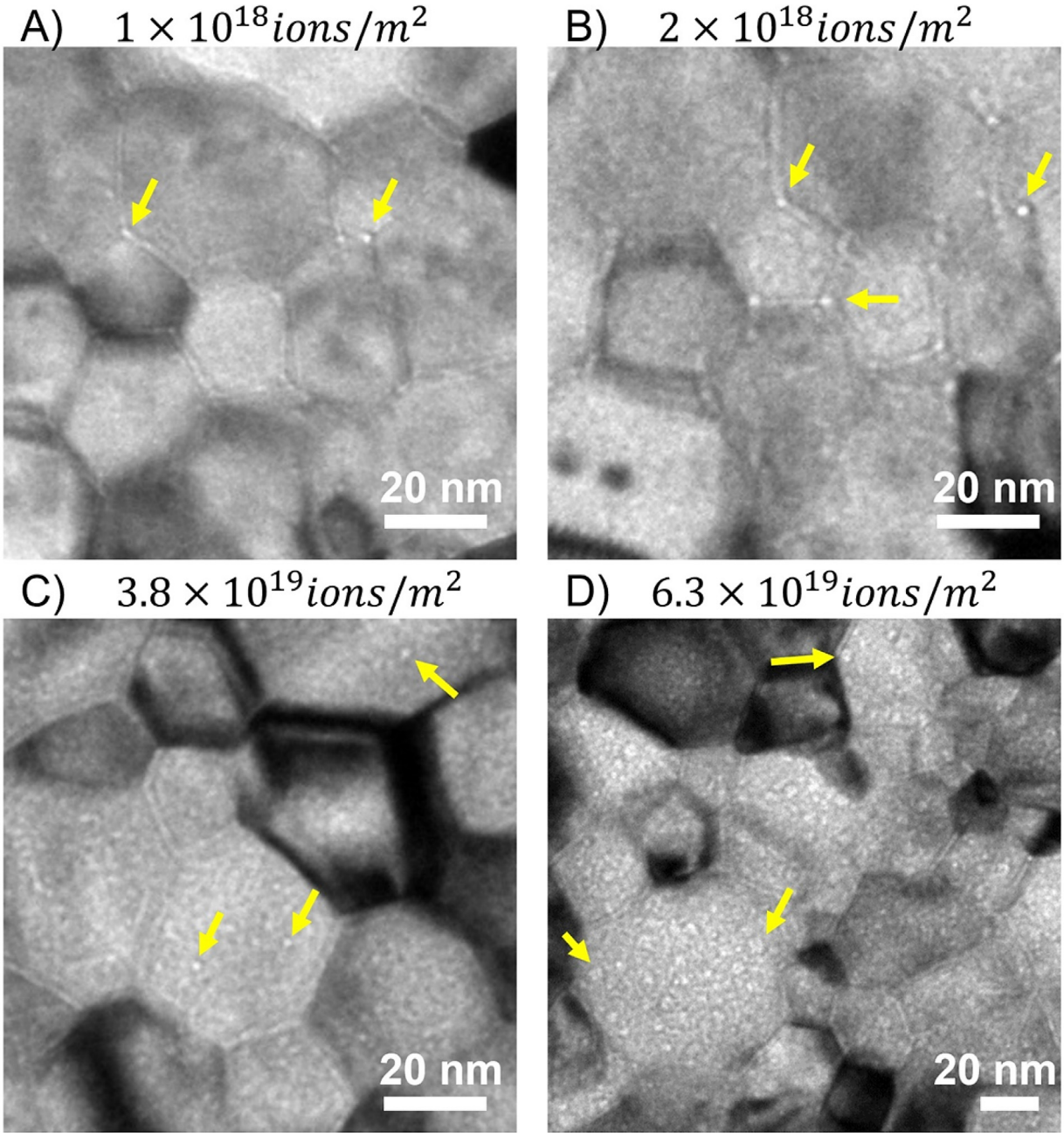

Fig. 13. Underfocus BF TEM images showing porosities in 1075K irradiated sample at A) 1×10^{18} *ions*/m^2, B) 2×10^{18} *ions*/m^2, C) 3.8×10^{19} *ions*/m^2, and D) 6.3×10^{19} *ions*/m^2. The yellow arrows point to porosities. BF images were not taken at the same locations. (For interpretation of the references to color in this figure, the reader is referred to the web version of this article).

3.5. Irradiation-induced defects under high temperature irradiation

The first assumption for the thermal spike model is that only defects created in the vicinity of grain boundaries contribute to the grain growth. This is true in the low temperature regime, where long-range thermal diffusion of irradiation-induced defects from the interior of the grain to the grain boundary is not significant. Therefore, the low temperature grain growth kinetics calculated using the thermal spike model is consistent with our experimental data. However, this assumption is not necessarily true for irradiation at higher temperatures, where the irradiation-induced point defects have enough mobility to travel to the grain boundaries during the experiment. Kaoumi et al. in [27] observed voids at grain boundaries for 500 keV irradiated Au thin films at 573 K, which is within the sink-dominated temperature regime, and thus pointed that the presence of point defect fluxes to grain boundaries should not be excluded during high temperature irradiation. Therefore, irradiation induced defects, such as porosities/voids and dislocation loops, were examined for the 1075 K irradiated UO_2 sample. The underfocused BF images in Fig. 13 clearly show typical porosities/voids found in the irradiated sample at different fluences. At low fluences, most of the porosities are found at the grain boundaries. Some of the voids are spherical shape and are found at the grain boundary triple junctions. At higher fluences, the porosities/voids were also found in the interior of the grains and eventually agglomerated into nanometer-size cavities spreading all over the samples. No porosities/voids denuded zone were observed near the grain boundaries. He et al. in [61] has shown

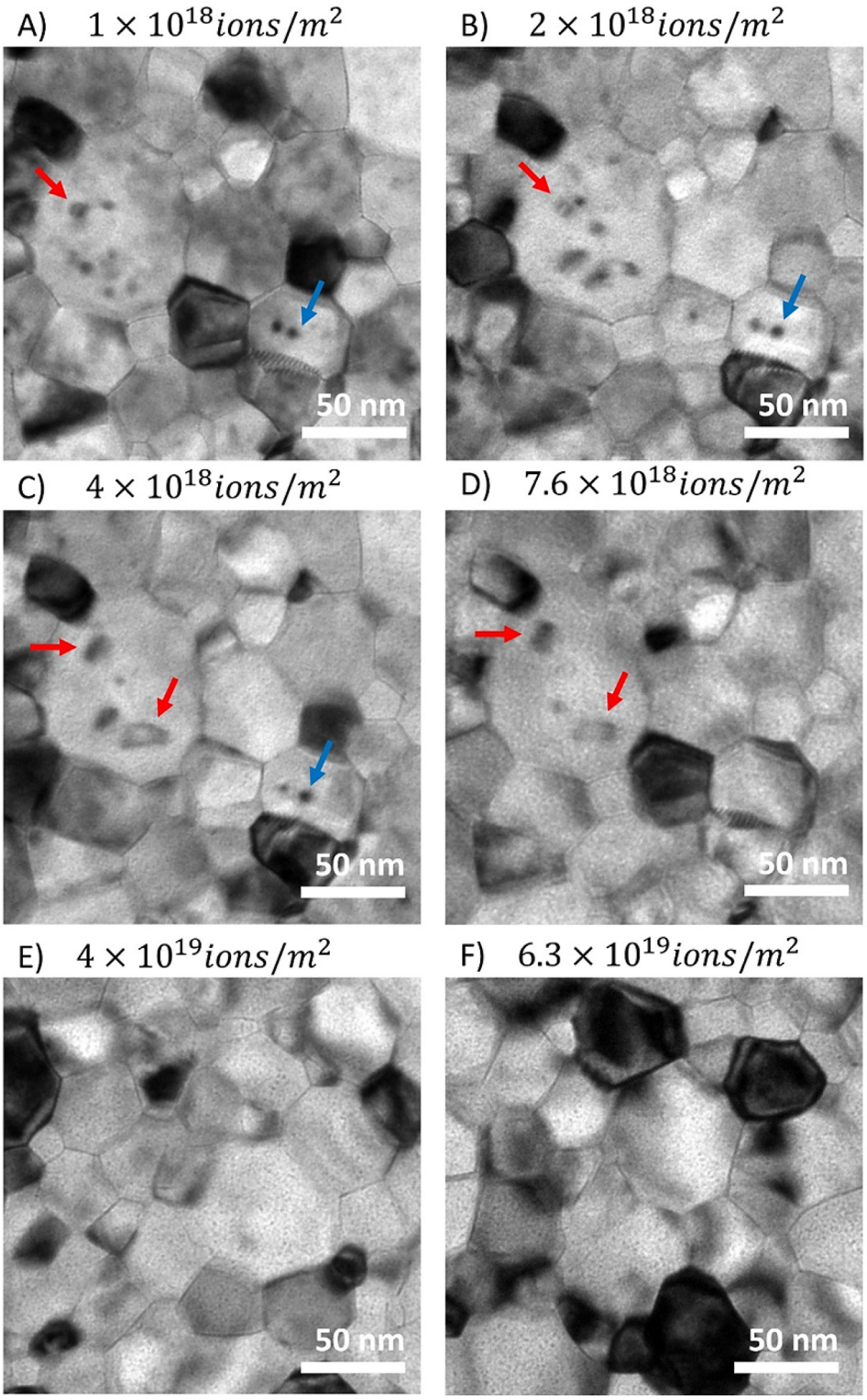

Fig. 14. Overfocus BF TEM images showing the evolution of dislocation loops in 1075K irradiated sample from (A) 1×10^{18} *ions*/m^2, (B) 2×10^{18} *ions*/m^2, (C) 4×10^{18} *ions*/m^2, (D) 7.6×10^{18} *ions*/m^2, (E) 4×10^{19} *ions*/m^2 to (F) 6.3×10^{19} *ions*/m^2. The red and blue arrows point to dislocation loops. Note images (A)–(D) were taken at the same location but images (E) and (F) were taken elsewhere. (For interpretation of the references to color in this figure, the reader is referred to the web version of this article).

the formation of intragranular Kr bubbles due to nucleation at vacancy clusters through a ballistic mixing process [62]. The average diameters of high temperature irradiation induced voids in the present study are about 3.3 ± 1.3 nm (maybe overestimated due to limited counts) large, which is also comparable with the reported bubble diameter after 1600°C annealing in [61]. Although other researchers have reported Kr bubbles during high temperature Kr ion irradiation, which can pin grain boundary motion, this can only help explain the early saturation of grain diameters in 1075 K irradiated sample as during the low temperature irradiations the Kr atoms are likely not mobile enough (and correspondingly, no bubbles are seen). The pinning effect of porosity on grain growth has

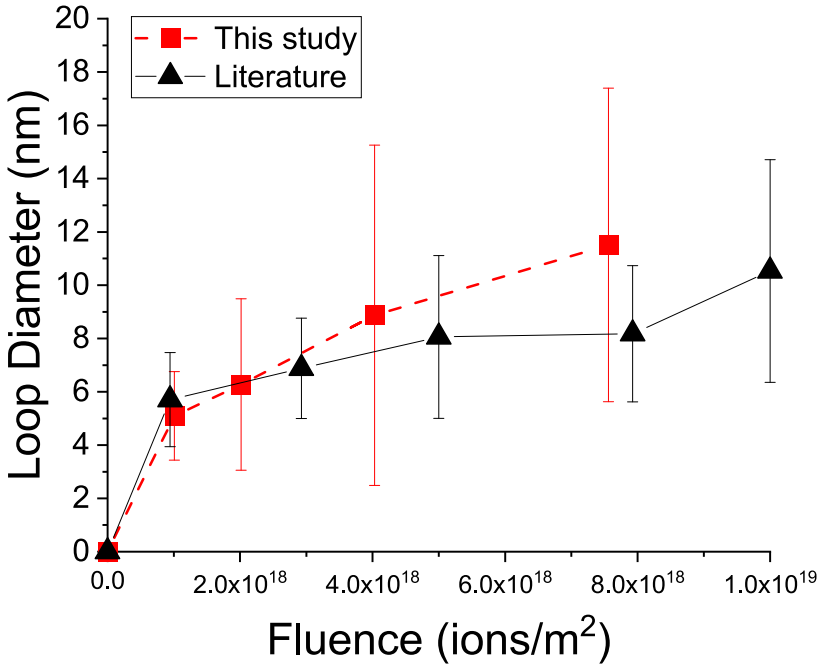

Fig. 15. Comparison of loop diameter measured in this study with literature values from He et al. [60].

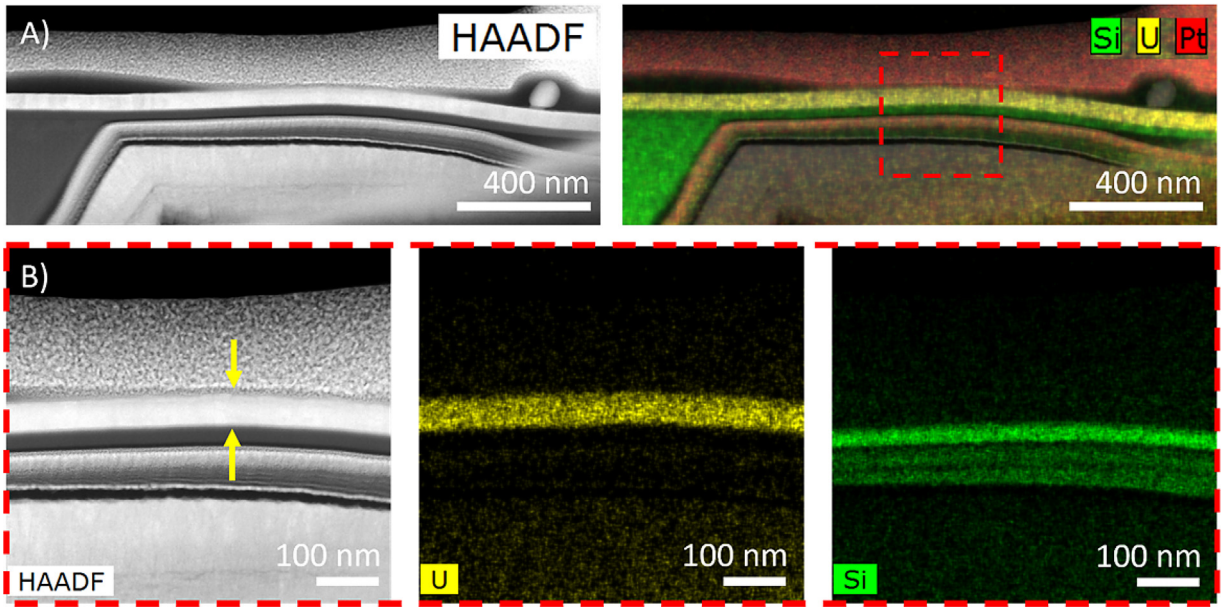

Fig. 16. HAADF images and EDS mapping showing the distribution of elements from the cross-section view of the 1075K irradiated thin film at (A) low magnification and (B) at high magnification. The UO_2 layer is highlighted between the two yellow arrows. (For interpretation of the references to color in this figure, the reader is referred to the web version of this article).

also been simulated by Ahmed et al. in [63] on CeO_2 at 1700 K using a phase field approach. The 2D simulations captured pores being picked up and break away from the migrating grain boundaries. The grain growth kinetics decreases as the porosity density increases.

In addition, irradiation-induced dislocation loops were also observed. Fig. 14 shows the evolution of a few typical dislocation loops found in the interior of the grain. Initially, isolated small loops were generated inside the grain. Later, some of the small loops started to agglomerate into larger loops (pointed by the red arrows). At the same time, some of the small loops (pointed by the blue arrow) created at low fluence (1×10^{18} ions/m^2) disappeared at slightly higher fluence (7.6×10^{18} ions/m^2). Similar evolution of dislocations has been reported by He et al. in [60], which shows small loops grow into bigger loops in polycrystalline UO_2 at 1075 K. To make a quantitative comparison, loop diameters measured at each fluence and plotted in Fig. 15. Despite a significant difference in the observed grain size in the two studies, the loop diameters in our nanocrystalline UO_2 follow a similar growing trend as the polycrystalline UO_2 used in [60]. The major difference is that big loops in polycrystalline UO_2 kept growing, eventually becoming dislocation lines, whereas the loops in our nanocrystalline UO_2 disappeared beyond a fluence of 1×10^{19} ions/m^2. The loop disappearing mechanism can be linked to point defects (interstitial) diffusion to grain boundaries and possibly loop elimination at the foil surface. As shown by He et al. in [60], sufficient interstitials may

migrate towards grain boundaries during high temperature irradiation so that the concentration of interstitials become low near the grain boundaries. This results in dislocation-denuded zone, which increases its width as a function of irradiation dose. At 1 $\times 10^{19}$ ions/m^2 fluence, the reported denuded zone is about 30 nm, which is almost the same as the grain size of our 1075 K irradiated samples at the same fluence. Thus, the enlarge dislocation-denuded zone could help explain the disappearing of dislocation loops at higher dose level. In addition, He et al. in [64] has attributed the shrinkage of dislocation loops during irradiation due to sample surface sink effects, which can absorb large amounts of interstitials and destabilize the loops. Lastly, there is a significant amount of intergranular porosities/voids/bubbles in the thin film. The loops can also be absorbed by these vacancy-type defects and eventually disappear.

Finally, we investigated whether the Si present in the sample substrate mixed in with the UO_2 during irradiation. Fig. 16 shows high angular annular dark field (HAADF)/Energy Dispersive Spectroscopy (EDS) images of a cross section of the thin film sample after irradiation. The UO_2 layer is shown as a yellow band (about 50 nm) on top of the Si wafer (green color). From the EDS maps in Fig. 16 (B), there is a clear separation of UO_2 layer and the Si wafer, without any mixture. Therefore, high temperature irradiation did not cause significant contamination of Si atoms in the UO_2 layer. The saturation of grain size is unlikely due to a solute drag force by Si atoms.

4. Conclusions

Nanocrystalline UO_2 thin films with an initial grain diameter about 10-15 nm were prepared by PLD onto silicon nitride membranes. Kr ion irradiated *in-situ* at temperatures ranging from 50 K to 1075 K as well as thermally annealed from 475 K to 1075 K were performed. The grain diameter and irradiation-induced defects were studied by transmission electron microscopy. The thermal spike model was applied to study the grain growth kinetics.

The main conclusions from this study are:

1. Grain growth in the UO_2 thin film occurred at all irradiation temperatures, including at 50 K.
2. In the temperature regime 50 – 475 K, grain growth occurred by interaction of the Kr ion irradiation with the previous microstructure likely through the thermal spike mechanism. Above this temperature thermal grain growth became increasingly important.
3. A machine learning method to measure grain diameter was developed which is consistent with the manual method, providing an efficient way to analyze a large number of TEM images for more reliable statistical results.
4. The low temperature results were well explained using the thermal spike model. At high temperature this model no longer applies and thermal grain growth with a resistive force became dominant.
5. Irradiation-induced defects, such as porosities/voids and dislocation loops, were observed in the larger grains formed in the sample irradiated at 1075 K.

Declaration of Competing Interest

The authors declare that they have no known competing financial interests or personal relationships that could have appeared to influence the work reported in this paper.

CRediT authorship contribution statement

Zefeng Yu: Methodology, Funding acquisition, Formal analysis, Writing – original draft, Writing – review & editing. **Xinyuan Xu:** Writing – original draft, Writing – review & editing. **Wei-Ying Chen:** Methodology, Writing – review & editing. **Yogesh Sharma:** Formal analysis, Writing – review & editing. **Xing Wang:** Writing – review & editing. **Aiping Chen:** Formal analysis, Writing – review & editing. **Christopher J. Ulmer:** Methodology, Conceptualization, Writing – review & editing. **Arthur T. Motta:** Funding acquisition, Supervision, Writing – review & editing.

Acknowledgment

This work was funded by the U.S. Department of Energy's Nuclear Engineering University Program project number 17-12797. Mr. Peter Baldo and Mr. Richard Sisson were thanked for operating the ion accelerator. The work at Los Alamos National Laboratory was supported by the NNSA's Laboratory Directed Research and Development Program and was performed, in part, at the Center for Integrated Nanotechnologies, an Office of Science User Facility operated for the U.S. Department of Energy Office of Science. Los Alamos National Laboratory, an affirmative action equal opportunity employer, is managed by Triad National Security, LLC for the U.S. Department of Energy's NNSA, under contract 89233218CNA000001. Z. Yu and A. Motta are CINT users and acknowledge the support from CINT users program. Y. S. acknowledges the support from the G. T. Seaborg Fellowship at Los Alamos National Laboratory. We also thank the IVEM staff in general, and especially Pete Baldo for helping to perform the *in-situ* ion irradiation experiments. Thanks Professor M. Tonks for discussion.

Supplementary materials

Supplementary material associated with this article can be found, in the online version, at doi:10.1016/j.actamat.2022.117856.

Appendix

To calculate the activation energy based on the thermal spike model, it is necessary to choose reasonable parameters for the values of the grain boundary energy, heat capacity and thermal conductivity. Figs. A1–A3 summarizes the literature data as a function of temperature. Tonks et al. in [2] has proposed the following equation

$$\gamma = \left(1.56 - 5.87 \times 10^{-4}\mathrm{T}\right) \pm 0.3\mathrm{J/m^2}$$

to represent the grain boundary energy as a function of temperature, T.

For the heat capacity and thermal conductivity, Fink in [51] has also proposed several equations to calculate the mean values at different temperatures. The best fit to the enthalpy data results in the heat capacity equation between 298.15 K and 3120 K as

$$\mathrm{C_p} = \frac{\mathrm{C_1}\theta^2 \mathrm{e}^{\frac{\theta}{\mathrm{T}}}}{\mathrm{T}^2\left(\mathrm{e}^{\frac{\theta}{\mathrm{T}}} - 1\right)^2} + 2\mathrm{C_2T} + \frac{\mathrm{C_3E_a e}^{-\frac{\mathrm{E_a}}{\mathrm{T}}}}{\mathrm{T}^2}$$

, where C_1= 81.61, θ = 548.68, C_2 = 2.29 $\times 10^{-3}$, C_3 = 2.36 $\times 10^{7}$, and E_a = 18531.71.

For the thermal conductivity, k, the equation used was initially recommend by Ronchi et al. in [48] as

$$\mathrm{k} = \frac{100}{7.5408 + 17.692\mathrm{t} + 3.6142\mathrm{t}^2} + \frac{6400}{\mathrm{t}^{5/2}} \exp\left(-\frac{16.35}{\mathrm{t}}\right)$$

where t = T (K)/1000 and k is the thermal conductivity of 95% dense UO_2 in W/m/K.

Since the temperature of the thermal spike pool is extremely high and the atoms within the cascade behave as liquid, the parameter values were chosen near the melting temperature of UO_2.

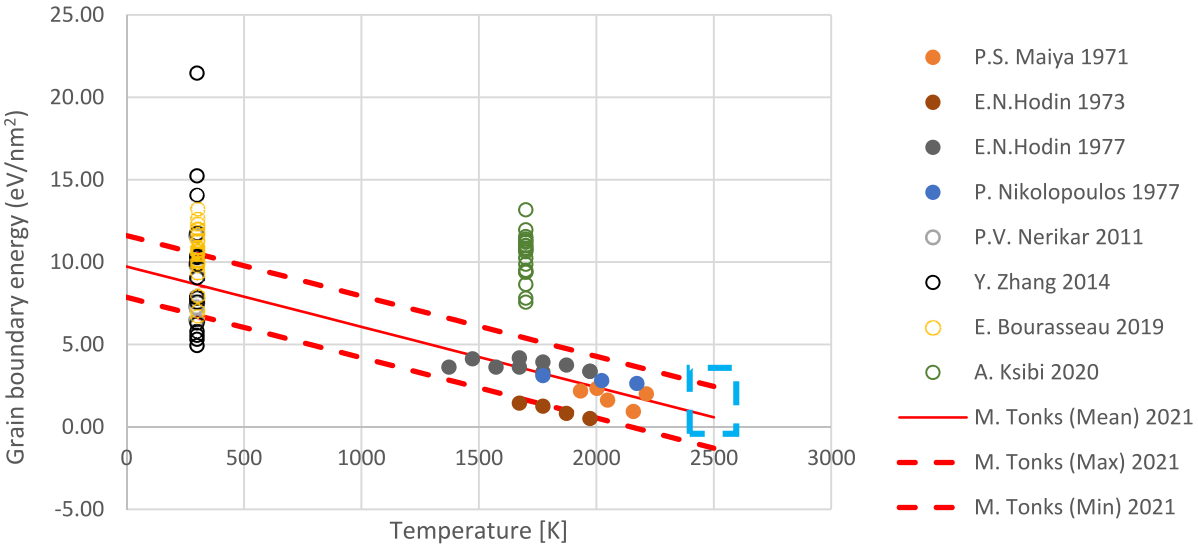

Fig. A1. Literature summary of grain boundary energies of UO_2 as a function of temperature [1,2,36–41]. The solid and dashed lines represent the mean grain boundary energy and the standard deviation calculated using the equation proposed in [2]. Blue dash box highlighted the range of the value used in thermal spike model. (For interpretation of the references to color in this figure, the reader is referred to the web version of this article).

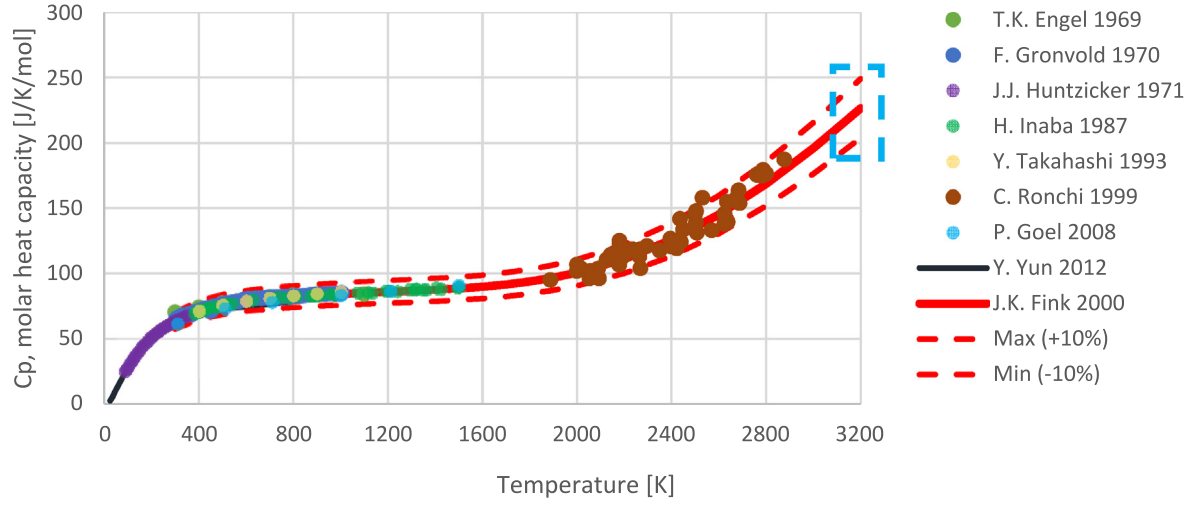

Fig. A2. Literature summary of molar heat capacity of UO_2 as a function of temperature [43–51]. The solid lines represent the mean molar heat capacity calculated using the equation proposed in [51]. The dash lines represent the possible range of the molar heat capacity covering all literatures values at different temperatures. Blue dash box highlighted the range of the value used in thermal spike model. (For interpretation of the references to color in this figure, the reader is referred to the web version of this article).

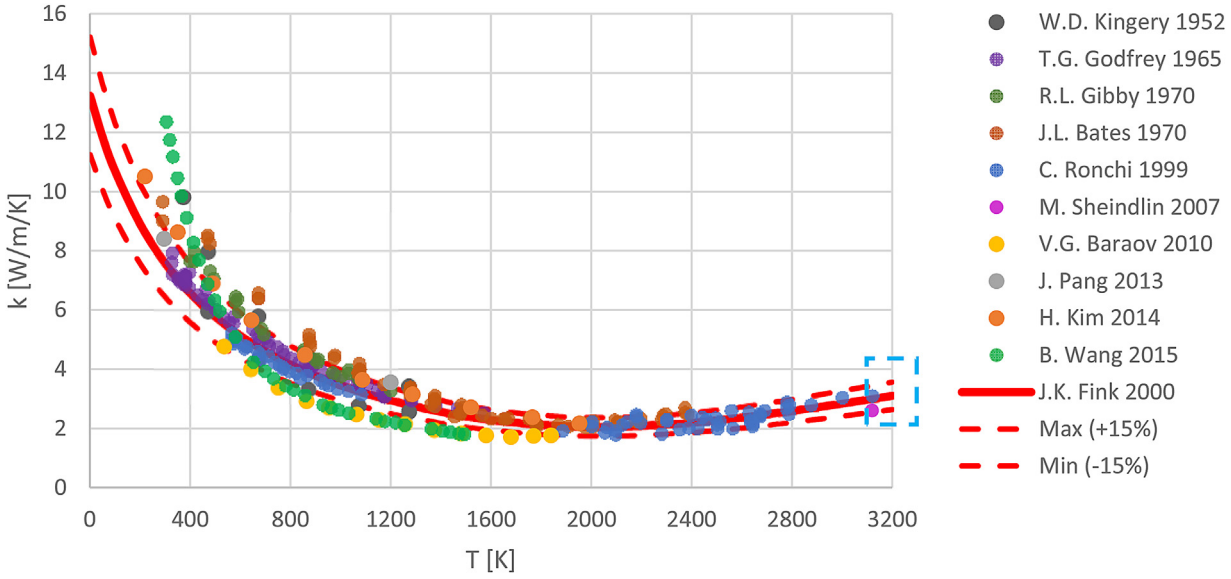

Fig. A3. Literature summary of thermal conductivity of UO_2 as a function of temperature [42,48,51–59]. The solid lines represent the mean thermal conductivity calculated using the equation proposed in [51]. The dash lines represent the possible range of the thermal conductivity. Blue dash box highlighted the range of the value used in thermal spike model. (For interpretation of the references to color in this figure, the reader is referred to the web version of this article).

References

[1] Y. Zhang, P.C. Millett, M.R. Tonks, X.M. Bai, S.B. Biner, Molecular dynamics simulations of intergranular fracture in UO_2 with nine empirical interatomic potentials, J. Nucl. Mater. 452 (2014) 296–303, doi:10.1016/j.jnucmat.2014.05.034.

[2] M.R. Tonks, P.C.A. Simon, J. Hirschhorn, Mechanistic grain growth model for fresh and irradiated UO_2 nuclear fuel, J. Nucl. Mater. 543 (2021) 152576, doi:10.1016/j.jnucmat.2020.152576.

[3] R.T. Michael, Z. Yongfeng, B. Aaron, B. Xian-Ming, Development of a grain boundary pinning model that considers particle size distribution using the phase field method, Model. Simul. Mater. Sci. Eng. 23 (2015) 45009. http://stacks.iop.org/0965-0393/23/i=4/a=045009.

[4] K. Shrestha, T. Yao, J. Lian, D. Antonio, M. Sessim, M.R. Tonks, K. Gofryk, The grain-size effect on thermal conductivity of uranium dioxide, J. Appl. Phys. (2019) 126, doi:10.1063/1.5116372.

[5] T. Watanabe, S.B. Sinnott, J.S. Tulenko, R.W. Grimes, P.K. Schelling, S.R. Phillpot, Thermal transport properties of uranium dioxide by molecular dynamics simulations, J. Nucl. Mater. 375 (2008) 388–396, doi:10.1016/j.jnucmat.2008.01.016.

[6] J.A. Turnbull, The effect of grain size on the swelling and gas release properties of uo2 during irradiation, J. Nucl. Mater. 50 (1974) 62–68. https://doi.org/10.1016/0022-3115(74)90061-0.

[7] D.U. Kim, S. Blondel, D.E. Bernholdt, P. Roth, F. Kong, D. Andersson, M.R. Tonks, B.D. Wirth, Modeling mesoscale fission gas behavior in UO_2 by directly coupling the phase field method to spatially resolved cluster dynamics, Mater. Theory 6 (2022) 7, doi:10.1186/s41313-021-00030-8.

[8] B. Gong, D. Frazer, T. Yao, P. Hosemann, M. Tonks, J. Lian, Nano- and micro-indentation testing of sintered UO_2 fuel pellets with controlled microstructure and stoichiometry, J. Nucl. Mater. 516 (2019) 169–177, doi:10.1016/j.jnucmat.2019.01.021.

[9] Y. Miao, T. Yao, J. Lian, S. Zhu, S. Bhattacharya, A. Oaks, A.M. Yacout, K. Mo, Nano-crystallization induced by high-energy heavy ion irradiation in UO_2, Scr. Mater. 155 (2018) 169–174, doi:10.1016/j.scriptamat.2018.04.006.

[10] W.W. Mullins, Two-dimensional motion of idealized grain boundaries, J. Appl. Phys. 27 (1956) 900–904, doi:10.1063/1.1722511.

[11] A. Michels, C.E. Krill, H. Ehrhardt, R. Birringer, D.T. Wu, Modelling the influence of grain-size-dependent solute drag on the kinetics of grain growth in nanocrystalline materials, Acta Mater. 47 (1999) 2143–2152, doi:10.1016/S1359-6454(99)00079-8.

[12] C.S. Olsen, UO_2 pore migration and grain growth kinetics, in: Proceedings of the Transactions of the International Conference on Structural Mechanics in Reactor Technology, C, Idaho Falls, 1979, p. 15.

[13] J.R. MacEWAN, V.B. Lawson, Grain growth in sintered uranium dioxide: II, columnar grain growth, J. Am. Ceram. Soc. 45 (1962) 42–46, doi:10.1111/j.1151-2916.1962.tb11027.x.

[14] T. Arima, K. Yoshida, K. Idemitsu, Y. Inagaki, I. Sato, Molecular dynamics analysis of diffusion of uranium and oxygen ions in uranium dioxide, IOP Conf. Ser. Mater. Sci. Eng. 9 (2010) 012003, doi:10.1088/1757-899x/9/1/012003.

[15] F. Glodeanu, I. Furtuna, A. Paraschiv, M. Paraschiv, Grain growth in high density UO_2, J. Nucl. Mater. 148 (1987) 351–352, doi:10.1016/0022-3115(87)90029-8.

[16] S. Van Aert, K.J. Batenburg, M.D. Rossell, R. Erni, G. Van Tendeloo, Three-dimensional atomic imaging of crystalline nanoparticles, Nature 470 (2011) 374–377, doi:10.1038/nature09741.

[17] I. Amato, R.L. Colombo, A.M. Protti, Influence of stoichiometry on the rate of grain growth of UO_2, J. Am. Ceram. Soc. 46 (1963) 407–407, doi:10.1111/j.1151-2916.1963.tb11762.x.

[18] I. Amato, R.L. Colombo, A.P. Balzari, Grain growth in pure and titania-doped uranium dioxide, J. Nucl. Mater. 18 (1966) 252–260, doi:10.1016/0022-3115(66)90166-8.

[19] F.A. Nichols, Theory of grain growth in porous compacts, J. Appl. Phys. 37 (1966) 4599–4602, doi:10.1063/1.1708102.

[20] J.B. Ainscough, B.W. Oldfield, J.O. Ware, Isothermal grain growth kinetics in sintered UO_2 pellets, J. Nucl. Mater. 49 (1973) 117–128, doi:10.1016/0022-3115(73)90001-9.

[21] R. Singh, Isothermal grain-growth kinetics in sintered UO_2 pellets, J. Nucl. Mater. 64 (1977) 174–178, doi:10.1016/0022-3115(77)90021-6.

[22] T. Kogai, R. Iwasaki, M. Hirai, In-pile and out-of-pile grain growth behavior of sintered UO_2 and (U, Gd)O_2 pellets, J. Nucl. Sci. Technol. 26 (1989) 744–751, doi:10.3327/jnst.26.744.

[23] T. Yao, K. Mo, D. Yun, S. Nanda, A.M. Yacout, J. Lian, Grain growth and pore coarsening in dense nano-crystalline UO_{2+x} fuel pellets, J. Am. Ceram. Soc. 100 (2017) 2651–2658, doi:10.1111/jace.14780.

[24] G.S. Was, Fundamentals of Radiation Materials Science: Metals and alloys, 2nd ed., Springer, New York, 2017, doi:10.1007/978-1-4939-3438-6.

[25] X. Zhang, K. Hattar, Y. Chen, L. Shao, J. Li, C. Sun, K. Yu, N. Li, M.L. Taheri, H. Wang, J. Wang, M. Nastasi, Radiation damage in nanostructured materials, Prog. Mater. Sci. 96 (2018) 217–321, doi:10.1016/j.pmatsci.2018.03.002.

[26] D. Kaoumi, A.T. Motta, R.C. Birtcher, Grain growth in nanocrystalline metal thin films under *in situ* ion-beam irradiation, in: Proceedings of the ASTM Special Technical Publication, 2008, pp. 206–218. 1492 STP.

[27] D. Kaoumi, A.T. Motta, R.C. Birtcher, A thermal spike model of grain growth under irradiation, J. Appl. Phys. 104 (2008) 1–13, doi:10.1063/1.2988142.

[28] E. Enriquez, G. Wang, Y. Sharma, I. Sarpkaya, Q. Wang, D. Chen, N. Winner, X. Guo, J. Dunwoody, J. White, A. Nelson, H. Xu, P. Dowden, E. Batista, H. Htoon, P. Yang, Q. Jia, A. Chen, Structural and optical properties of phase-pure UO_2, α-U_3O_8, and α-UO_3epitaxial thin films grown by pulsed laser deposition, ACS Appl. Mater. Interfaces 12 (2020) 35232–35241, doi:10.1021/acsami.0c08635.

[29] L. LYNDS, W.A. YOUNG, J.S. MOHL, G.G. LIBOWITZ, X-Ray and Density Study of Nonstoichiometry in Uranium Oxides, in: 1963: pp. 58–65. https://doi.org/10.1021/ba-1964-0039.ch005.

[30] L.F. He, J. Pakarinen, M.A. Kirk, J. Gan, A.T. Nelson, X.M. Bai, A. El-Azab, T.R. Allen, Microstructure evolution in Xe-irradiated UO_2 at room temperature, Nucl. Instrum. Methods Phys. Res. Sect. B Beam Interact. Mater. Atoms 330 (2014) 55–60, doi:10.1016/j.nimb.2014.03.018.

[31] R.E. Stoller, M.B. Toloczko, G.S. Was, A.G. Certain, S. Dwaraknath, F.A. Garner, On the use of SRIM for computing radiation damage exposure, Nucl. Instrum. Methods Phys. Res. Sect. B Beam Interact. Mater. Atoms 310 (2013) 75–80, doi:10.1016/j.nimb.2013.05.008.

[32] O. Ronneberger, P. Fischer, T. Brox, U-Net: Convolutional Networks for Biomedical Image Segmentation, in: Lect. Notes Comput, Sci. (Including Subser. Lect. Notes Artif. Intell. Lect. Notes Bioinformatics) (2015) 234–241. https://doi.org/10.1007/978-3-319-24574-4_28.

[33] J.E. Burke, D. Turnbull, Recrystallization and grain growth, Prog. Met. Phys. (1952) 3, doi:10.1016/0502-8205(52)90009-9.

[34] D. Kaoumi, A.T. Motta, R.C. Birtcher, Grain growth in Zr-Fe thin films during *in situ* ion irradiation in a TEM, Nucl. Instrum. Methods Phys. Res. Sect. B Beam Interact. Mater. Atoms 242 (2006) 490–493, doi:10.1016/j.nimb.2005.08.158.
[35] C.J. Ulmer, W.Y. Chen, D.E. Wolfe, A.T. Motta, *In-situ* ion irradiation induced grain growth in nanocrystalline ceria, J. Nucl. Mater. 545 (2021) 152688, doi:10.1016/j.jnucmat.2020.152688.
[36] P.S. Maiya, Surface diffusion, surface free energy, and grain-boundary free energy of uranium dioxide, J. Nucl. Mater. 40 (1971) 57–65, doi:10.1016/0022-3115(71)90116-4.
[37] E.N. Hodkin, M.G. Nicholas, Surface and interfacial properties of non-stoichiometric uranium dioxide, J. Nucl. Mater. 67 (1977) 171–180, doi:10.1016/0022-3115(77)90172-6.
[38] P. Nikolopoulos, S. Nazaré, F. Thümmler, Surface, grain boundary and interfacial energies in UO_2 and UO_2-Ni, J. Nucl. Mater. 71 (1977) 89–94, doi:10.1016/0022-3115(77)90191-X.
[39] P.V. Nerikar, K. Rudman, T.G. Desai, D. Byler, C. Unal, K.J. McClellan, S.R. Phillpot, S.B. Sinnott, P. Peralta, B.P. Uberuaga, C.R. Stanek, Grain boundaries in uranium dioxide: Scanning electron microscopy experiments and atomistic simulations, J. Am. Ceram. Soc. 94 (2011) 1893–1900, doi:10.1111/j.1551-2916.2010.04295.x.
[40] E. Bourasseau, A. Mouret, P. Fantou, X. Iltis, R.C. Belin, Experimental and simulation study of grain boundaries in UO_2, J. Nucl. Mater. 517 (2019) 286–295, doi:10.1016/j.jnucmat.2019.02.033.
[41] A. Ksibi, E. Bourasseau, X. Iltis, D. Drouan, M. Gaudet, A. Germain, A. Pena, G. Lapertot, J.P. Brison, R.C. Belin, Experimental and numerical assessment of grain boundary energies in polycrystalline uranium dioxide, J. Eur. Ceram. Soc. 40 (2020) 4191–4201, doi:10.1016/j.jeurceramsoc.2020.04.041.
[42] T.G. Godfrey, W. Fulkerson, T.G. Kollie, J.P. Moore, D.L. McElroy, Thermal Conductivity of Uranium Dioxide from -57° to 1100°C by a Radial Heat Flow Technique, J. Am. Ceram. Soc. 48 (1965) 297–305, doi:10.1111/j.1151-2916.1965.tb14745.x.
[43] T.K. Engel, The heat capacities of Al_2O_3, UO_2 and PuO_2 From 300 To 1100 °K, J. Nucl. Mater. 31 (1969) 211–214, doi:10.1016/0022-3115(69)90194-9.
[44] F. Grønvold, N.J. Kveseth, A. Sveen, J. Tichý, Thermodynamics of the UO_{2+x} phase I. Heat capacities of $UO_{2.017}$ and $UO_{2.254}$ from 300 to 1000 K and electronic contributions, J. Chem. Thermodyn. 2 (1970) 665–679, doi:10.1016/0021-9614(70)90042-X.
[45] J.J. Huntzicker, E.F. Westrum, The magnetic transition, heat capacity, and thermodynamic properties of uranium dioxide from 5 to 350 K, J. Chem. Thermodyn. 3 (1971) 61–76, doi:10.1016/S0021-9614(71)80067-8.
[46] H. Inaba, K. Naito, M. Oguma, Heat capacity measurement of $U_{1-y}Gd_yO_2$ ($0.00 \leqq y \leqq 0.142$) from 310 to 1500 K, J. Nucl. Mater. 149 (1987) 341–348, doi:10.1016/0022-3115(87)90536-8.
[47] Y. Takahashi, M. Asou, High-temperature heat-capacity measurements on (U, Gd)O_2 by drop calorimetry and DSC, J. Nucl. Mater. 201 (1993) 108–114, doi:10.1016/0022-3115(93)90164-T.
[48] C. Ronchi, M. Sheindlin, M. Musella, G.J. Hyland, Thermal conductivity of uranium dioxide up to 2900 K from simultaneous measurement of the heat capacity and thermal diffusivity, J. Appl. Phys. 85 (1999) 776–789, doi:10.1063/1.369159.
[49] P. Goel, N. Choudhury, S.L. Chaplot, Atomistic modeling of the vibrational and thermodynamic properties of uranium dioxide, UO_2, J. Nucl. Mater. 377 (2008) 438–443, doi:10.1016/j.jnucmat.2008.03.020.
[50] Y. Yun, D. Legut, P.M. Oppeneer, Phonon spectrum, thermal expansion and heat capacity of UO_2 from first-principles, J. Nucl. Mater. 426 (2012) 109–114, doi:10.1016/j.jnucmat.2012.03.017.
[51] J.K. Fink, Thermophysical properties of uranium dioxide, J. Nucl. Mater. 279 (2000) 1–18, doi:10.1016/S0022-3115(99)00273-1.
[52] B.T. Wang, J.J. Zheng, X. Qu, W.D. Li, P. Zhang, Thermal conductivity of UO_2 and PuO_2 from first-principles, J. Alloy. Compd. 628 (2015) 267–271, doi:10.1016/j.jallcom.2014.12.204.
[53] W.D. Kingery, J. Francl, R.L. Coble, T. Vasilos, Thermal conductivity: X, data for several pure oxide materials corrected to zero porosity, J. Am. Ceram. Soc. 37 (1954) 107–110, doi:10.1111/j.1551-2916.1954.tb20109.x.
[54] M. Sheindlin, D. Staicu, C. Ronchi, L. Game-Arnaud, B. Remy, A. Degiovanni, Experimental determination of the thermal conductivity of liquid UO_2 near the melting point, J. Appl. Phys. 101 (2007), doi:10.1063/1.2721091.
[55] V.G. Baranov, Y.N. Devyatko, A.V. Tenishev, A.V. Khlunov, O.V. Khomyakov, New method for determining the temperature dependence of the thermal conductivity coefficient of dielectrics in a pulse experiment, Inorg. Mater. Appl. Res. 1 (2010) 167–173, doi:10.1134/S2075113310020164.
[56] R.L. Gibby, The effect of plutonium content on the thermal conductivity of (U, Pu)O_2 solid solutions, J. Nucl. Mater. 38 (1971) 163–177, doi:10.1016/0022-3115(71)90040-7.
[57] J.L. Bates, High-temperature thermal conductivity of “round robin, uranium dioxide (BNWL–1431), 1970. https://www.osti.gov/servlets/purl/4084378.
[58] J.W.L. Pang, W.J.L. Buyers, A. Chernatynskiy, M.D. Lumsden, B.C. Larson, S.R. Phillpot, Phonon lifetime investigation of anharmonicity and thermal conductivity of UO_2 by neutron scattering and theory, Phys. Rev. Lett. 110 (2013) 1–5, doi:10.1103/PhysRevLett.110.157401.
[59] H. Kim, M.H. Kim, M. Kaviany, Lattice thermal conductivity of UO_2 using ab-initio and classical molecular dynamics, J. Appl. Phys. (2014) 115, doi:10.1063/1.4869669.
[60] L.F. He, M. Gupta, M.A. Kirk, J. Pakarinen, J. Gan, T.R. Allen, *In situ* TEM observation of dislocation evolution in polycrystalline UO_2, JOM 66 (2014) 2553–2561, doi:10.1007/s11837-014-1186-6.
[61] L. He, X.M. Bai, J. Pakarinen, B.J. Jaques, J. Gan, A.T. Nelson, A. El-Azab, T.R. Allen, Bubble evolution in Kr-irradiated UO_2 during annealing, J. Nucl. Mater. 496 (2017) 242–250, doi:10.1016/j.jnucmat.2017.09.036.
[62] R.A. Enrique, P. Bellon, Phase stability under irradiation in alloys with a positive heat of mixing: effective thermodynamics description, Phys. Rev. B Condens. Matter Mater. Phys. 60 (1999) 14649–14659, doi:10.1103/PhysRevB.60.14649.
[63] K. Ahmed, T. Allen, A. El-Azab, Phase field modeling for grain growth in porous solids, J. Mater. Sci. 51 (2016) 1261–1277, doi:10.1007/s10853-015-9107-9.
[64] L.F. He, M. Gupta, C.A. Yablinsky, J. Gan, M.A. Kirk, X.M. Bai, J. Pakarinen, T.R. Allen, *In situ* TEM observation of dislocation evolution in Kr-irradiated UO_2 single crystal, J. Nucl. Mater. 443 (2013) 71–77, doi:10.1016/j.jnucmat.2013.06.050.